bioRxiv preprint doi: https://doi.org/10.1101/2021.11.18.469197; this version posted April 29, 2022. The copyright holder for this preprint (which was not certified by peer review) is the author/funder. All rights reserved. No reuse allowed without permission.

Nonquantal Transmission at the Vestibular Hair Cell-Calyx Synapse: K_{LV} Currents Modulate Fast Electrical and Slow K^+ Potentials in the Synaptic Cleft

Aravind Chenrayan Govindaraju[1], Imran H. Quraishi[2], Anna Lysakowski[3], Ruth Anne Eatock[4], Robert M. Raphael[5]

[1]Applied Physics Graduate Program, Department of Bioengineering, Rice University, Houston, TX; ORCID 0000-0002-2306-8599

[2]Department of Neurology, Yale University School of Medicine, New Haven, CT; ORCID 0000-0003-2859-7446

[3]Department of Anatomy and Cell Biology, University of Illinois at Chicago, IL; ORCID 0000-0001-6259-0294

[4]Department of Neurobiology, University of Chicago, Chicago, IL; ORCID 0000-0001-7547-2051

[5]Department of Bioengineering, Rice University, Houston, TX; ORCID 0000-0003-4986-7847

Author for correspondence:
Robert M. Raphael
Dept. of Bioengineering, MS 142
Rice University
Houston, TX
rraphael@rice.edu

The authors declare no competing interests.

bioRxiv preprint doi: https://doi.org/10.1101/2021.11.18.469197; this version posted April 29, 2022. The copyright holder for this preprint (which was not certified by peer review) is the author/funder. All rights reserved. No reuse allowed without permission.

Abstract

Vestibular hair cells transmit information about head position and motion across synapses to primary afferent neurons. At some of these synapses, the afferent neuron envelopes the hair cell, forming an enlarged synaptic terminal called a calyx. The vestibular hair cell-calyx synapse supports a mysterious form of electrical transmission that does not involve gap junctions termed nonquantal transmission (NQT). The NQT mechanism is thought to involve the flow of ions from the pre-synaptic hair cell to the post-synaptic calyx through low-voltage-activated channels driven by changes in cleft [K^+] as K^+ exits the hair cell. However, this hypothesis has not been tested with a quantitative model and the possible role of an electrical potential in the cleft has remained speculative. Here we present a computational model that captures salient experimental observations of NQT and identifies overlooked features that corroborate the existence of an electrical potential (ϕ) in the synaptic cleft. We show that changes in cleft ϕ reduce transmission latency and illustrate the relative contributions of both cleft [K^+] and ϕ to the gain and phase of NQT. We further demonstrate that the magnitude and speed of NQT depend on calyx morphology and that increasing calyx height reduces action potential latency in the calyx afferent. These predictions are consistent with the idea that the calyx evolved to enhance NQT and speed up vestibular signals that drive neural circuits controlling gaze, balance, and orientation.

bioRxiv preprint doi: https://doi.org/10.1101/2021.11.18.469197; this version posted April 29, 2022. The copyright holder for this preprint (which was not certified by peer review) is the author/funder. All rights reserved. No reuse allowed without permission.

Significance Statement

The ability of the vestibular system to drive the fastest reflexes in the nervous system depends on rapid transmission of mechanosensory signals at vestibular hair cell synapses. In mammals and other amniotes, afferent neurons form unusually large calyx terminals on certain hair cells, and communication at these synapses includes nonquantal transmission (NQT), which avoids the synaptic delay of quantal transmission. We present a quantitative model that shows how NQT depends on the extent of the calyx covering the hair cell and attributes the short latency of NQT to changes in synaptic cleft electrical potential caused by current flowing through open potassium channels in the hair cell. This previously undescribed mechanism may act at other synapses.

bioRxiv preprint doi: https://doi.org/10.1101/2021.11.18.469197; this version posted April 29, 2022. The copyright holder for this preprint (which was not certified by peer review) is the author/funder. All rights reserved. No reuse allowed without permission.

Introduction

The vestibular inner ear transduces head motion and drives the fastest known reflexes in the nervous system, including the vestibulo-ocular reflex (Huterer and Cullen 2002) and the vestibulo-collic reflex (Colebatch and Rosengren 2019). These reflexes support gaze, balance, and orientation (Cullen 2019) and are essential for locomotion. The first synapses in these pathways are from mechanosensory hair cells onto primary afferent nerve terminals. In mammals and other amniotes, many vestibular afferent terminals form prominent cup-like structures, termed calyces around specialized type I hair cells (Wersäll 1956; Gulley and Bagger-Sjöbäck 1979; Lysakowski and Goldberg 2004). Transmission at these synapses has been inferred to be exceptionally fast (McCue and Guinan 1994), prompting speculation that it includes a direct, electrical component in addition to glutamate exocytosis from synaptic vesicles (quantal transmission). Electrical transmission typically involves gap junctions (Nielsen et al. 2012) but gap junctions are not present at vestibular hair cell-calyx (VHCC) synapses (Gulley and Bagger-Sjöbäck 1979; Ginzberg 1984; Yamashita and Ohmori 1991). Nonetheless, electrophysiological recordings from calyx-bearing afferents established that an additional mode of transmission can occur with or without quantal transmission (Yamashita and Ohmori 1990; Holt et al. 2007; Songer and Eatock 2013; Highstein et al. 2014; Contini et al. 2017). This mysterious form of transmission came to be called Nonquantal Transmission (NQT).

NQT has been suggested to be mediated by the flow of ions from the pre-synaptic hair cell to the post-synaptic calyx through low-voltage-activated K^+ (K_{LV}) channels (Eatock 2018), but how pre-synaptic currents alter the driving forces of post-synaptic currents has not been well understood. A key challenge for understanding NQT at the VHCC synapse is the lack of experimental access to the synaptic cleft and pre-and post-synaptic membranes. Early models (Chen 1995; Goldberg 1996) recognized that the elongated cleft space between the type I hair cell and enveloping calyx structure could provide increased electrical resistance and limit the diffusion of ions. In these formulations, K^+ that enters hair cells during mechanotransduction is extruded into the synaptic cleft, leading to K^+ accumulation and a change in the K^+ chemical potential that drives membrane currents. Changes in cleft electrical potential were not thought to be significant. In support of these models, subsequent experimental results emphasized the role of K^+ accumulation (Lim et al. 2011; Contini et al. 2012, 2017, 2020; Spaiardi et al. 2020). Other processes were also suggested, including accumulation of glutamate (Dalet et al. 2012; Sadeghi et al. 2014) and protons (Highstein et al. 2014). However, the existence and role of an electrical potential in the synaptic cleft has remained a matter of speculation. A clear biophysical explanation for how NQT

bioRxiv preprint doi: https://doi.org/10.1101/2021.11.18.469197; this version posted April 29, 2022. The copyright holder for this preprint (which was not certified by peer review) is the author/funder. All rights reserved. No reuse allowed without permission.

occurs and how currents and driving forces interact quantitatively at the VHCC synapse has not yet been presented.

To discern the biophysical basis of NQT, we have developed a detailed computational model of the VHCC synapse based on the anatomy of the afferent calyx terminal and the properties of ion channels and transporters expressed in the hair cell, calyx terminal and afferent fiber. Simulated responses of the VHCC model to hair bundle deflection and voltage-clamp steps accurately predict experimental data. Such validation gives us confidence in the model's predictions for sites with no experimental data, notably the inaccessible synaptic cleft. Results show that NQT at the VHCC synapse depends on the geometry of the calyx, involves modulation of both the electrical potential and K^+ concentration in the synaptic cleft, and is mediated primarily by currents through low-voltage-activated potassium (K_{LV}) conductances that take different forms in the presynaptic and postsynaptic membranes ("$g_{K,L}$" channels and K_V7 channels, respectively). A major outcome of the model is the recognition of features in post-synaptic responses (Songer and Eatock 2013; Contini et al. 2020) as evidence for changes in electrical potential in the synaptic cleft during NQT.

Changes in extracellular electrical potential have long been known to play a role in ephaptic coupling, a general term for coupling via proximity of neural elements (Jefferys 1995; Faber and Pereda 2018). Ephaptic coupling has been implicated in signal transmission in the retina (Vroman et al. 2013; Warren et al. 2016), cerebellum (Han et al. 2018, 2020), hippocampus (Chiang et al. 2019), and heart (Veeraraghavan et al. 2014; Gourdie 2019). At the VHCC synapse, however, the importance of changes in cleft electrical potential have gone unrecognized despite the extensive synaptic cleft which is formed by the close apposition of the pre-synaptic (hair cell) and post-synaptic (afferent) membranes. The VHCC model we develop is able to decouple electrical and K^+ potentials and demonstrate that change in cleft electrical potential is necessary to explain: 1) the short latency of NQT; 2) the experimentally observed phase response of NQT (Songer and Eatock 2013); 3) fast retrograde events in the hair cell during post-synaptic action potentials (Contini et al. 2017); and 4) the shape of the fast current response of the calyx to voltage changes in the hair cell (Contini et al. 2020). By showing how the magnitude and speed of NQT depends on the calyx, our model supports the idea that calyx evolved to support faster transmission in response to increased locomotory challenges presented by the tetrapod transition from water to land (Eatock 2018; Curthoys et al. 2019).

bioRxiv preprint doi: https://doi.org/10.1101/2021.11.18.469197; this version posted April 29, 2022. The copyright holder for this preprint (which was not certified by peer review) is the author/funder. All rights reserved. No reuse allowed without permission.

Key Abbreviations

AP: action potential

MET: mechanoelectrical transduction

NQT: Nonquantal Transmission

VHCC: Vestibular Hair Cell-Calyx

Electrical potentials (with respect to perilymph):

ϕ_H electric potential in the hair cell

ϕ_{SC} electrical potential in the synaptic cleft

ϕ_C electric potential in calyx

Transmembrane Voltages

V_H voltage across the basolateral hair cell membrane, $(\phi_H - \phi_{SC})$

V_{CIF} voltage across calyx inner face membrane, $(\phi_C - \phi_{SC})$

Concentrations and ionic potentials

$[K^+]_{SC}$ K^+ concentration in the synaptic cleft

$[Na^+]_{SC}$ Na^+ concentration in the synaptic cleft

E_K Equilibrium potential for K^+ (K^+ potential) across hair cell or calyx membranes

bioRxiv preprint doi: https://doi.org/10.1101/2021.11.18.469197; this version posted April 29, 2022. The copyright holder for this preprint (which was not certified by peer review) is the author/funder. All rights reserved. No reuse allowed without permission.

General Description of the Model

The model has been developed for an afferent calyx around a single type I hair cell ("simple calyx-only terminal") based on the geometry of a vestibular hair cell and calyx from the striolar zone of the rat utricle, see **Fig. 1** and **Supplementary Information (*SI*), Fig. S1**. The morphology of vestibular hair cells and calyces is highly conserved within particular zones of vestibular epithelia (Lysakowski and Goldberg 1997, 2008) and thus the model is representative of simple VHCC synapses in the striolar zone.

The model incorporates ion channels and transporters identified from experimental studies of type I hair cells and associated afferents to simulate the voltage response of the calyx to mechanical and electrical stimuli: hair bundle deflection and hair cell voltage steps. Most of the parameters in the model are from published literature (**SI Tables S5, S6 and S7**); methods are provided for the unpublished data (**SI Experimental Methods**). The model was created to understand how currents and driving forces interact at the VHCC synapse during nonquantal transmission (NQT) – a change in the calyx potential in response to a change in hair cell potential that does not involve exocytosis of packets (vesicles or quanta) of neurotransmitter nor gap junctions. We do not consider quantal transmission, as the goal is to understand NQT as an independent phenomenon. In addition, mammalian calyces recorded in vitro often show only NQT. The predictions of the model are compared to experimental results in which only NQT was present at the synapse. Simulations used physiological parameters from experimental data performed at room temperature.

The key parameters of interest are changes that occur in the electrical potential and K^+ concentration of the synaptic cleft, which is not experimentally accessible. The model incorporates capacitive and resistive currents across both the pre-synaptic hair cell and post-synaptic calyx membranes and uses continuity and electro-diffusion equations to describe the relationship between currents, electrical potentials and ion concentrations in the synaptic cleft. Using a finite element approach and COMSOL Multiphysics® software, we simulate the effects of changes in electrical potential in each model compartment and how these changes represent the mechanosensory signal as it travels from one compartment to the next. In the synaptic cleft, spatiotemporal changes in both electrical potential and ion concentrations are simulated and result in spatially varying driving forces for currents along the basal-to-apical extent of hair cell and calyx inner face membranes. Initial and boundary conditions and full details on channel kinetics are provided in **SI**. The overall geometry, localization of ion channels and other relevant variables are presented in **Fig. 1**.

bioRxiv preprint doi: https://doi.org/10.1101/2021.11.18.469197; this version posted April 29, 2022. The copyright holder for this preprint (which was not certified by peer review) is the author/funder. All rights reserved. No reuse allowed without permission.

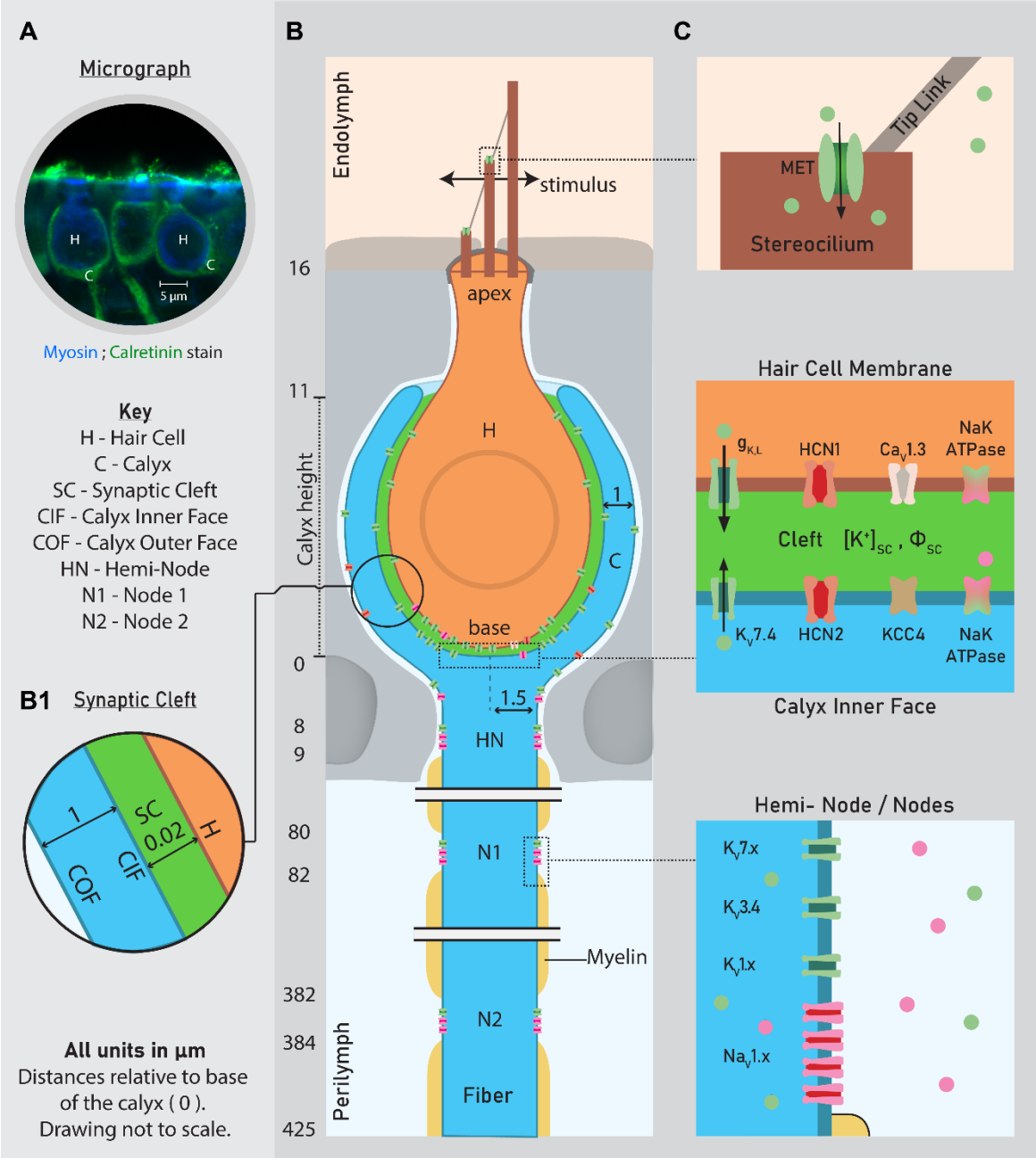

Fig. 1 – Illustration of the VHCC synapse depicting the distribution of ion channels and transporters in the hair cell (H), synaptic cleft (SC), calyx (C) and afferent fiber (F).

A, Confocal micrograph of type I hair cells (H, blue myosin immunolabel) within calyces (C, green calretinin immunolabel). Long-Evans adult rat utricle, striolar zone.

B, Geometry of a type I hair cell-calyx synapse from central/striolar zones of rodent vestibular organs, and the dimensions used in the model. A 2D curve representing the hair cell, synaptic cleft and calyx was generated (**SI, Fig. S1**) based on measurements from Lysakowski et al. 2011, their Fig. 2C. Long-Evans adult rat crista, central zone. Dimensions were comparable (within 10%) to those of hair cells and calyces in A**. B1,** Cleft and calyx width.

C, The ion channel types at different key locations in the model. See **SI, Tables S6** and **S7** for sources of channel kinetics and distributions. $\boldsymbol{\phi_{SC}}$, electrical potential in the synaptic cleft; $[\boldsymbol{K}^+]_{\boldsymbol{SC}}$, K^+ concentration in the synaptic cleft.

bioRxiv preprint doi: https://doi.org/10.1101/2021.11.18.469197; this version posted April 29, 2022. The copyright holder for this preprint (which was not certified by peer review) is the author/funder. All rights reserved. No reuse allowed without permission.

Results

We use the VHCC model to delineate biophysical events and driving forces that underlie NQT and describe their effects on the mechanosensory signal communicated to the calyx terminal of the afferent neuron. We first describe the resting state of the VHCC compartments, then responses to step bundle deflections. In each condition, we provide the model's output in terms of: 1) electrical potentials relative to a distant ground for the hair cell (ϕ_H), synaptic cleft (ϕ_{SC}), and calyx (ϕ_C); 2) trans-membrane voltages for the hair cell (V_H) and the calyx inner face (V_{CIF}) membranes facing the synaptic cleft; 3) K^+ and Na^+ concentrations in the synaptic cleft ($[K^+]_{SC}$, $[Na^+]_{SC}$); and 4) key ion-channel currents across each membrane. The contributions of ϕ_{SC} and $[K^+]_{SC}$ are then analyzed separately to determine their roles in driving pre- and post-synaptic currents and thus NQT. We then compare model results to published data showing NQT during sinusoidal hair bundle displacement and paired voltage clamp recordings from hair cells and calyces to identify features that corroborate the existence and role of an electrical potential in the cleft. Finally, to understand the extent to which NQT depends on calyx morphology, we analyze the effect of calyx height on the electrical and potassium potentials in the cleft (ϕ_{SC}, E_K) and the response latency of the calyx.

Resting state of the system. The model was fully defined with no free parameters that required additional estimation. From the initial values and boundary conditions, we calculated the resting currents, ion concentrations, electrical potentials, and membrane voltages, using the stationary solver in COMSOL (***SI, Computational Methods***). At rest, the MET channels had a 10% open probability, corresponding to -43 pA of current. The model produced hair cell and calyx resting potentials (ϕ_H: –78 mV, ϕ_C: –65 mV) that are consistent with reported resting ϕ_H and ϕ_C (Rennie and Correia 1994; Rennie et al. 1996; Rüsch and Eatock 1996; Chen and Eatock 2000; Sadeghi et al. 2014; Spaiardi et al. 2017). Model resting output values for which there are no experimental data for comparison are: ϕ_{SC} at the base of the synapse, +2 mV; $[K^+]_{SC}$ and $[Na^+]_{SC}$ at the base of the synapse, 7 mM and 129 mM, respectively. The non-zero value for ϕ_{SC} emerges from currents at rest carried by the same ion channels and transporters that participate in stimulus-evoked NQT.

These results were taken as the initial conditions from which to determine, with the time-dependent solver (COMSOL), changes in response to a stimulus. In all figures, the values at t = 0 show conditions at rest.

Synaptic response to a step displacement of the hair bundle. In **Fig. 2**, we illustrate the simulated response of sequential stages in the VHCC model to a positive (excitatory) step (+1 µm) of hair bundle

bioRxiv preprint doi: https://doi.org/10.1101/2021.11.18.469197; this version posted April 29, 2022. The copyright holder for this preprint (which was not certified by peer review) is the author/funder. All rights reserved. No reuse allowed without permission.

displacement at 50 ms followed by a negative (inhibitory) displacement (–1 µm). The stimulus (**Fig. 2A**) is bundle displacement viewed from above relative to resting position, taken mid-way up the bundle and parallel to the plane of the epithelium (**Fig. 1B**, 'stimulus'). The mechanotransduction current (I_{MET}) elicited by bundle stimulation is shown in **Fig. 2B**. Positive bundle displacement evoked a peak inward I_{MET} of ~400 pA, and the negative step reduced I_{MET} to 0. These changes in I_{MET} depolarized and hyperpolarized ϕ_H (**Fig. 2C**, modeled by **SI Eq. S2**), respectively, and altered hair cell basolateral (pre-synaptic) currents (**Fig. 3**). This model does not consider transducer adaptation, such that any decay (adaptation) of I_{MET} is driven by changes in ϕ_H, which changes the driving force on I_{MET}. NQT manifests as a change in calyx potential, ϕ_C (**Fig. 2G**), in response to changes in hair cell potential, ϕ_H. For this bundle deflection, the NQT-induced change in ϕ_C was large enough to trigger an action potential (AP) in the calyx which is in turn transmitted retrogradely by NQT back to the hair cell, showing up as transients at each stage (**Fig. 2B-F, arrowheads** and **Fig. 3A-C, vertical dashed line and asterisks**).

Predicted Changes in Cleft Electrical Potential, Na^+ and K^+ Concentrations and Transmembrane Voltages.

The model permits simulation of biophysical properties of the cleft microenvironment, which is not experimentally accessible. During NQT, the synaptic cleft potential, ϕ_{SC}, changes as shown in **Fig. 2E,E1.** The dynamic changes in ϕ_{SC} (modeled by **SI Eq. S5**) allow calculation of pre-synaptic ($V_H = \phi_H - \phi_{SC}$) and post-synaptic ($V_{CIF} = \phi_C - \phi_{SC}$) trans-membrane voltages. V_H (**Fig. 2D**) and V_{CIF} (**Fig. 2F**) differ by ϕ_{SC} from the intracellular potentials with respect to ground (ϕ_H and ϕ_C, **Fig. 2C,G**).

Figure 2E shows the predicted changes in $[K^+]_{SC}$ and $[Na^+]_{SC}$ in the synaptic cleft at its base: K^+ accumulation was accompanied by Na^+ depletion, as predicted by a previous electrodiffusion model of the type I-calyx that considered the effect of the cleft on the hair cell receptor potential (Soto et al. 2002). In our VHCC model, changes in ion concentrations in the cleft are caused by: 1) altered ionic currents, mostly through channels in the pre-synaptic and post-synaptic membranes; and 2) the axial electro-diffusion of ions from the source (ion channels in the depth of the cleft) to the sink (apical edges of the calyx) (**Fig. 1**, and **SI Eqs. S3,S4**).

Synaptic cleft electrical potential, ϕ_{SC}, rises much faster than the synaptic K^+ potential. To more clearly illustrate the variables responsible for the speed of NQT we show the dynamic changes in ϕ_H (**Fig. 2C1**) and ϕ_C (**Fig. 2G1**), V_H and V_{CIF} (**Fig. 2D1,F1**), and synaptic cleft potential, ϕ_{SC} (**Fig. 2E1**) at the onset

bioRxiv preprint doi: https://doi.org/10.1101/2021.11.18.469197; this version posted April 29, 2022. The copyright holder for this preprint (which was not certified by peer review) is the author/funder. All rights reserved. No reuse allowed without permission.

of the +1 µm step. We also plot the equilibrium potential of K^+, (E_K), which reflects changes in synaptic cleft potassium level, $[K^+]_{SC}$ (**Fig. 2E1**).

Differences in the time courses of stimulus-evoked changes in ϕ_{SC}, E_K, and V_{CIF} provide key insight into the driving forces for NQT. At the onset of the positive step, the synaptic cleft potential, ϕ_{SC}, rises from 1.9 mV to +6 mV in 0.43 ms, 8-fold faster than the time for E_K to rise the same amount (-79.9 mV to -75.8 mV) (**Fig. 2E1**). The rise in E_K is also slow compared to the change in V_{CIF} (**Fig. 2F1**). This provides an important insight into the mechanism of NQT that has not been previously recognized: ϕ_{SC} provides the initial driving force for change in the post-synaptic membrane current, and only later does change in E_K make a significant contribution. This difference arises because fewer ions are needed to change ϕ_{SC} than E_K. **Fig. 2C1-F1** highlight how changes in ϕ_{SC} (**Fig. 2E1**) affect the magnitude of V_H (**Fig. 2D**) and the magnitude and direction of V_{CIF} (**Fig. 2F**). At step onset, V_{CIF} hyperpolarizes while ϕ_C depolarizes (**Fig. 2F1,G1, asterisks)**. The hyperpolarization of V_{CIF} occurs because the fast depolarization of the cleft (ϕ_{SC}) is larger than the fast depolarization of the intracellular calyx potential (ϕ_C) making $V_{CIF} = (\phi_C - \phi_{SC})$ negative. The subsequent slow rise in V_{CIF} follows the depolarization of ϕ_C which results from the slow increase in $[K^+]_{SC}$ and E_K. That V_{CIF} and ϕ_C are different and can change in opposing directions makes it apparent that voltage across the calyx inner and outer face membranes can be different despite the common intracellular potential. While the VHCC model results agree with experiments showing that changes in synaptic cleft *[K^+]* affect both hair cell and calyx signals (Lim et al. 2011; Contini et al. 2012, 2017; Spaiardi et al. 2020), the model further shows a pivotal role for the synaptic cleft potential in reducing transmission latency. The independent contributions of ϕ_{SC} and $[K^+]_{SC}$ to NQT are analyzed later.

bioRxiv preprint doi: https://doi.org/10.1101/2021.11.18.469197; this version posted April 29, 2022. The copyright holder for this preprint (which was not certified by peer review) is the author/funder. All rights reserved. No reuse allowed without permission.

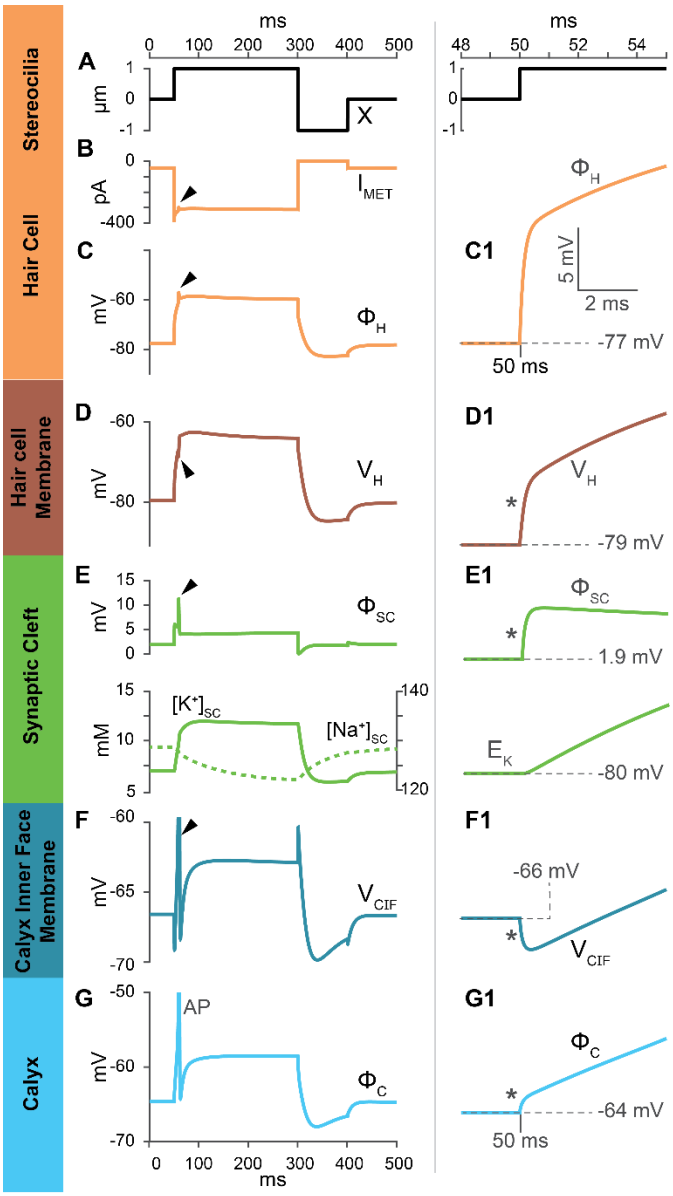

Fig. 2 – Propagation of the mechanosensory signal evoked by hair bundle displacement, illustrating dynamic changes in electrical and K^+ potentials at each stage.

A, Displacement (X) of the hair bundle: +1-µm, 250-ms step, beginning at t=50 ms and followed by negative step to -1-µm (300-ms) step. **B-G,** Responses to full stimulus, progressing from I_{MET} (B) to calyx postsynaptic potential (G). **Arrowheads** point to the retrograde echo of a calyx action potential that was stimulated by anterograde transmission. **C-G,** Values shown are at the base of the synapse. **C1-G1**, Responses in C-G to +step on expanded time scale (between 48 and 55 ms).

B, I_{MET}.

C,C1, Hair cell receptor potential (electrical potential re: ground, ϕ_H) rises rapidly.

D,D1, Voltage across the basolateral hair cell membrane (V_H) rises rapidly but is smaller than ϕ_H by the cleft potential ($V_H = \phi_H - \phi_{SC}$).

E, $[K^+]_{SC}$ (*solid line*; left axis) rises while $[Na^+]_{SC}$ (*dotted line*; right axis) falls.

E1, Synaptic cleft electrical potential relative to ground (ϕ_{SC}) rises much faster than K^+ potential (E_K) for $[K^+]_{SC}$.

F,G, Voltage across calyx inner face membrane ($V_{CIF} = \phi_C - \phi_{SC}$) rapidly hyperpolarizes (**F,F1**) and then reverses as ϕ_C depolarizes (**G,G1**), ultimately producing a calyceal AP (**G**). Note that after +step onset, fast components (*****) of V_H (**D1**) and V_{CIF} (**F1**) have opposite polarities and same time course as fast rise in ϕ_{SC} (**E1**).

bioRxiv preprint doi: https://doi.org/10.1101/2021.11.18.469197; this version posted April 29, 2022. The copyright holder for this preprint (which was not certified by peer review) is the author/funder. All rights reserved. No reuse allowed without permission.

Contributions of Different Ion Channels to Nonquantal Transmission

The synaptic cleft is a dynamic system where electric potentials, ion concentrations and ionic currents interact. The changes in cleft electrical potential and ion concentrations shown in **Fig. 2** are driven by currents through voltage-sensitive ion channels (see **SI, Table S6** for kinetics) on the hair cell basolateral membrane and on the calyx inner face, and in turn modulate these currents (**Fig. 3**). NQT is bidirectional: we first describe the roles of key channels during anterograde (hair cell to calyx) NQT and later discuss retrograde (calyx to hair cell) NQT.

Currents through open $g_{K,L}$ channels respond very rapidly to hair cell depolarization. The large low-voltage-activated K^+ conductance "$g_{K,L}$" is a distinctive feature of type I vestibular hair cells (Correia and Lang 1990; Rennie and Correia 1994; Rüsch and Eatock 1996). At the resting bundle position (t<50 ms, **Figs. 2** and **3**) before the step, V_H is only slightly positive (~1 mV) of E_K (-80 mV; **Fig. 2E1**). Despite this small driving force, $g_{K,L}$ has a large open probability (~50%) because of its very negative activation range and carries significant outward K^+ current, $I_{K,L}$, into the cleft (**Fig. 3A**). At the onset of the positive step, ϕ_H and V_H depolarize faster than E_K (**Fig. 2C1-E1**). Since $g_{K,L}$ is already significantly open, the increase in driving force ($V_H - E_K$) instantaneously increases $I_{K,L}$ (**Fig. 3A**), altering both ϕ_{SC} and $[K^+]_{SC}$. $I_{K,L}$ is largely sustained; a modest decrease (~10%, from +350 pA to +317 pA) reflects the reduction in driving force as $[K^+]_{SC}$ increases and E_K depolarizes (**Fig. 3B**).

In **Fig. 3** we have presented local potentials at the base of the synapse and whole-cell ionic currents. However, the VHCC model has the ability to calculate the spatio-temporal distributions of these variables. In our model conditions, the net $I_{K,L}$ was never inward (negative). However, by using the model to examine membrane currents as functions of location along the cleft, we noticed that inward $I_{K,L}$ can occur locally at the base of the hair cell during a negative step if V_H becomes negative to E_K (**SI Fig. S2**). These results support the idea that $g_{K,L}$ may under certain conditions carry inward K^+ currents into the hair cell and aid in K^+ clearance (Spaiardi et al. 2020).

Figure 3 shows that the current through $g_{K,L}$ is fast, large, and non-inactivating, so that it closely follows the hair bundle stimulus. Since $g_{K,L}$ is high in the resting state, the receptor potential-induced change in $I_{K,L}$ is not delayed by ion channel activation and is near instantaneous. $I_{K,L}$ rapidly changes the cleft electrical potential (**Fig. 3B,** *bottom trace*), which in turn rapidly alters currents through low-voltage-activated potassium (K_{LV}) channels in the calyx inner face membrane.

bioRxiv preprint doi: https://doi.org/10.1101/2021.11.18.469197; this version posted April 29, 2022. The copyright holder for this preprint (which was not certified by peer review) is the author/funder. All rights reserved. No reuse allowed without permission.

Excitatory stimuli decrease K_V7 current into the synaptic cleft from the calyx. The postsynaptic K_{LV} conductances include the K_V7 family of voltage-gated channels (Hurley et al. 2006). The VHCC model permits quantitative characterization of the role of these channels in modulating $[K^+]_{SC}$ and ϕ_{SC} during NQT, which has not previously been clear. According to the model, at resting membrane potential (V_{CIF} = –68 mV), outward current through partly open (29%) K_V7 channels on the calyx inner face supplies K^+ to the synaptic cleft, helping to set resting levels of $[K^+]_{SC}$ and ϕ_{SC}. During positive bundle displacement, changes in V_{CIF} and E_K across the calyx inner face membrane (**Fig. 3B**) slightly reduce outward K_V7 currents into the synaptic cleft (**Fig. 3A,** I_{Kv7}) except during the calyx action potential (AP) where outward K_V7 currents rise (**Fig. 3A,** I_{Kv7}, asterisk).

Synaptic HCN channels establish resting conditions but have minimal effect on $[K^+]_{SC}$ and ϕ_{SC} during NQT. Hyperpolarization-activated cyclic-nucleotide-gated (HCN) channels are found on both sides of the VHCC synapse. Type I hair cells primarily express HCN1 channel subunits (Horwitz et al. 2011) and vestibular afferent neurons primarily express HCN2 subunits (Horwitz et al. 2014). Model results show that under physiological concentrations and potentials, HCN channels support a net inward current in both cells, mediated by influx of Na^+ ions, that is 10-100-fold smaller than outward K^+ currents through $g_{K,L}$ and K_V7 channels (**Fig. 3A**). In the model, we localized HCN1 to the hair cell and HCN2 to the calyx and found that both HCN channels had smaller open probabilities (HCN1-18%; HCN2-8%) than K_{LV} channels ($g_{K,L}$ - 50%; K_V7 - 29%) at rest (V_H= -79 mV; V_{CIF} = –68 mV) and contributed very small currents to either positive (**Fig. 3A**) or negative (**SI Fig. S2**) step responses. This difference relative to K_{LV}-associated currents is explained by the HCN channels' smaller whole-cell conductance values (**see SI, Table S6**), their hyperpolarized voltage range of activation, and their mixed cationic currents (K^+ and Na^+) moving in opposite directions. In the model, both HCN1 and HCN2 channels, along with the Na^+/K^+-ATPase, contribute to the regulation of $[K^+]$ and $[Na^+]$ in the synaptic cleft (**Fig. 2E**). Blocking HCN channels has been experimentally shown to block NQT (Contini et al. 2017), but only under conditions that artificially favor HCN channels: i.e., when the calyx was held at –100 mV, an unphysiological (substantially negative to E_K) condition at which most K_V7 channels would be closed and most HCN channels would be open.

Retrograde transmission from calyx to hair cell. The VHCC model naturally captures retrograde transmission (**Fig. 2B-F, arrowheads**), defined as a change in hair cell potential caused by a change in calyx potential. This is especially pronounced during NQT-induced postsynaptic action potentials that occur for sufficiently large hair bundle displacements. An action potential in the fiber (**Fig. 2G; Fig. 3C**) causes the calyx inner face membrane to depolarize (**Fig. 3B,** V_{CIF}) and increases outward current, primarily through

bioRxiv preprint doi: https://doi.org/10.1101/2021.11.18.469197; this version posted April 29, 2022. The copyright holder for this preprint (which was not certified by peer review) is the author/funder. All rights reserved. No reuse allowed without permission.

K_V7 channels (**Fig. 3A**; compare K_V7 and HCN2); ϕ_{SC} rises (**Fig. 3B**); V_H becomes more negative (**Fig. 3B**); outward K^+ currents from the hair cell, primarily through $g_{K,L}$ channels, decrease (**Fig. 3A,** see $g_{K,L}$ and HCN1); and the hair cell potential, ϕ_H, depolarizes (**Fig. 2C, arrowhead; Fig 3B**). The fast component of retrograde transmission is mediated by changes in ϕ_{SC} and not E_K (**Fig. 3, asterisks**). These results indicate that fast retrograde events seen in electrophysiological recordings of the hair cell and calyx (Contini et al. 2017) are caused by changes in electrical potential in the synaptic cleft. It has been suggested that the bidirectional nature of nonquantal transmission, which our VHCC model captures, could be used to modulate the sensitivity of both the calyx and the hair cell (Holt et al. 2017).

bioRxiv preprint doi: https://doi.org/10.1101/2021.11.18.469197; this version posted April 29, 2022. The copyright holder for this preprint (which was not certified by peer review) is the author/funder. All rights reserved. No reuse allowed without permission.

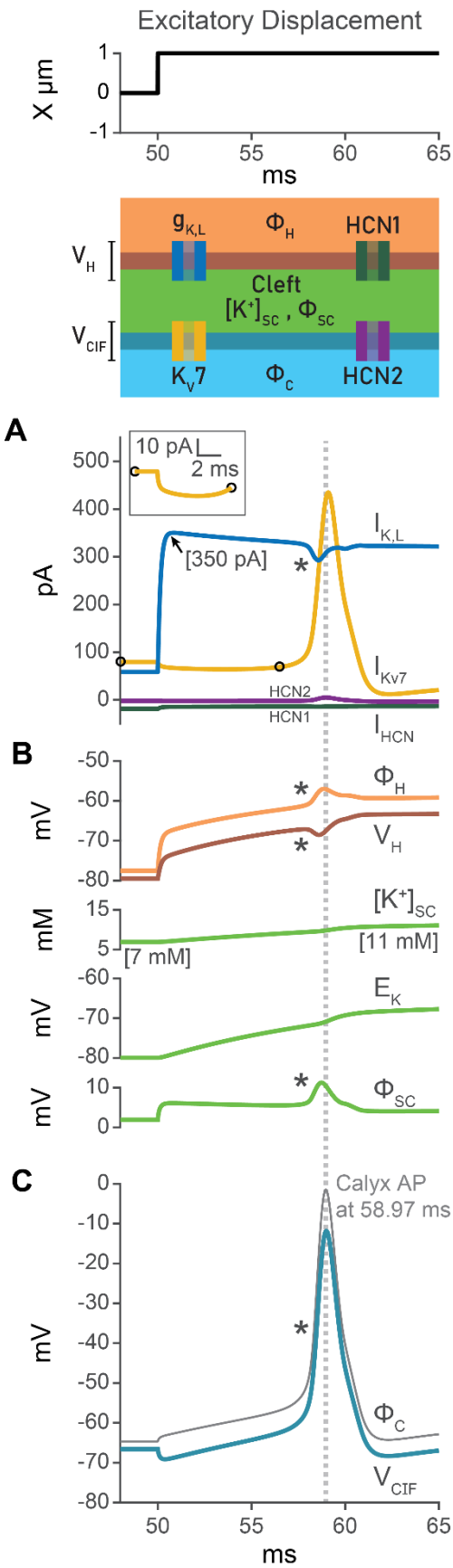

Fig. 3 – Ionic currents during hair bundle stimulation and Retrograde NQT of a calyx AP to the hair cell. During excitatory step bundle displacements (top), ionic currents (**A**), primarily through hair cell $g_{K,L}$ and calyx K_V7, are affected by and affect cleft properties (ϕ_{SC} and $[K^+]_{SC}$; **B**). Anterograde NQT evokes a single AP in the calyx (gray line, **C**; peak shown by dashed line). **Asterisks** in A-C show the retrograde influence of the calyx AP on hair cell and calyx currents (A), hair cell and cleft properties (B), and calyx (C) voltages.

A, Net currents through $g_{K,L}$ (hair cell, blue), K_V7 (calyx, gold) and HCN channels (hair cell, brown, and calyx, purple) in response to the first 15 ms of the +1-µm step. **A inset,** expanded view of K_V7 current decrease at + step onset.

B, ϕ_H, V_H, $[K^+]_{SC}$, E_K and ϕ_{SC} at the base of the synapse during excitatory stimulus, showing that fast retrograde transmission to the hair cell occurs through ϕ_{SC} and not E_K. See **asterisks**.

C, V_{CIF} (cyan) and ϕ_C (gray, featuring the calyx AP) at the base of the synapse during excitatory stimuli.

bioRxiv preprint doi: https://doi.org/10.1101/2021.11.18.469197; this version posted April 29, 2022. The copyright holder for this preprint (which was not certified by peer review) is the author/funder. All rights reserved. No reuse allowed without permission.

Role of the Synaptic Cleft in Nonquantal Transmission: $\boldsymbol{\phi_{SC}}$ and $[\boldsymbol{K}^+]_{SC}$

The predictions of the VHCC model agree with experimental observations (Lim et al. 2011; Contini et al. 2012, 2017, 2020; Spaiardi et al. 2020) that support the hypothesis that K^+ currents through the basolateral membrane of the type I hair cell modulate $[K^+]_{SC}$ (Chen 1995; Goldberg 1996) and change E_K to affect pre- and post-synaptic currents. The model further shows that modulation of ϕ_{SC} also alters both pre-synaptic and post-synaptic ionic currents but on a substantially faster time scale. What are the relative contributions of ϕ_{SC} and $[K^+]_{SC}$ to NQT? Are both mechanisms necessary? What advantages do they provide? To answer these questions, we use the VHCC model to isolate ϕ_{SC} and $[K^+]_{SC}$ during both step and sinusoidal bundle displacements.

Isolation of the contributions of $\boldsymbol{\phi_{SC}}$ and $[\boldsymbol{K}^+]_{SC}$ during step bundle displacements. We mathematically define two conditions: ϕ_{SC} modulation and $[K^+]_{SC}$ modulation. The ϕ_{SC} modulation-only condition is set by fixing $[K^+]_{SC}$ and $[Na^+]_{SC}$ at 5 mM and 140 mM, respectively, while ϕ_{SC} is allowed to vary as a function of ionic currents (**SI Eqs. S8-10**). The $[K^+]_{SC}$ modulation-only condition is set by fixing ϕ_{SC} at 0 mV and allowing $[K^+]_{SC}$ and $[Na^+]_{SC}$ to vary as functions of the ionic currents (**SI Eqs. S11-13**). **Figure 4** illustrates how ϕ_{SC} and $[K^+]_{SC}$ separately and together shape the calyx potential (**Fig. 4B1,B2**) and its time derivative (**Fig. 4C1,C2**) at the onset of 2 positive bundle displacements. The ϕ_{SC} modulation reduced the latency of the calyx potential by 1.8 ms (0.3 μm step) and 1.5 ms (1 μm step). **Figures 4C1,C2** show the considerably greater rate of change in calyx potential, $\frac{d\phi_C}{dt}$, for the ϕ_{SC}condition compared to the $[K^+]_{SC}$ condition, and how both combine.

Figure 4 also shows that $[K^+]_{SC}$ modulation is responsible for the slow component of the rise in calyx potential. When ϕ_{SC} and $[K^+]_{SC}$ are allowed to vary concomitantly, both fast and slow components are seen. Comparing the rise of ϕ_C in the $[K^+]_{SC}$-only and 'Both' conditions clearly shows that change in ϕ_{SC} confers a ~1-2 ms advance to the calyx response (**Fig. 4B**). Thus, the modulation of ϕ_{SC} enables faster signal transmission between hair cell and calyx. The modulation of $[K^+]_{SC}$, although slower, results in a larger depolarization of the calyx. For these inputs to the VHCC model, both mechanisms together did not trigger spiking for smaller hair bundle deflections, but both were necessary to elicit spiking for the larger deflection. In the presence of an action potential, the response of the model at each stage is influenced by currents at the hemi-nodes and nodes of the afferent fiber (**SI, Eqs. S6, S7** and **Table S6**). ϕ_C (**Fig. 4B2**) closely resembles experimental whole-cell recordings of the voltage response of a rat utricular calyx to positive step displacements (Songer and Eatock 2013 – their Fig. 5A).

bioRxiv preprint doi: https://doi.org/10.1101/2021.11.18.469197; this version posted April 29, 2022. The copyright holder for this preprint (which was not certified by peer review) is the author/funder. All rights reserved. No reuse allowed without permission.

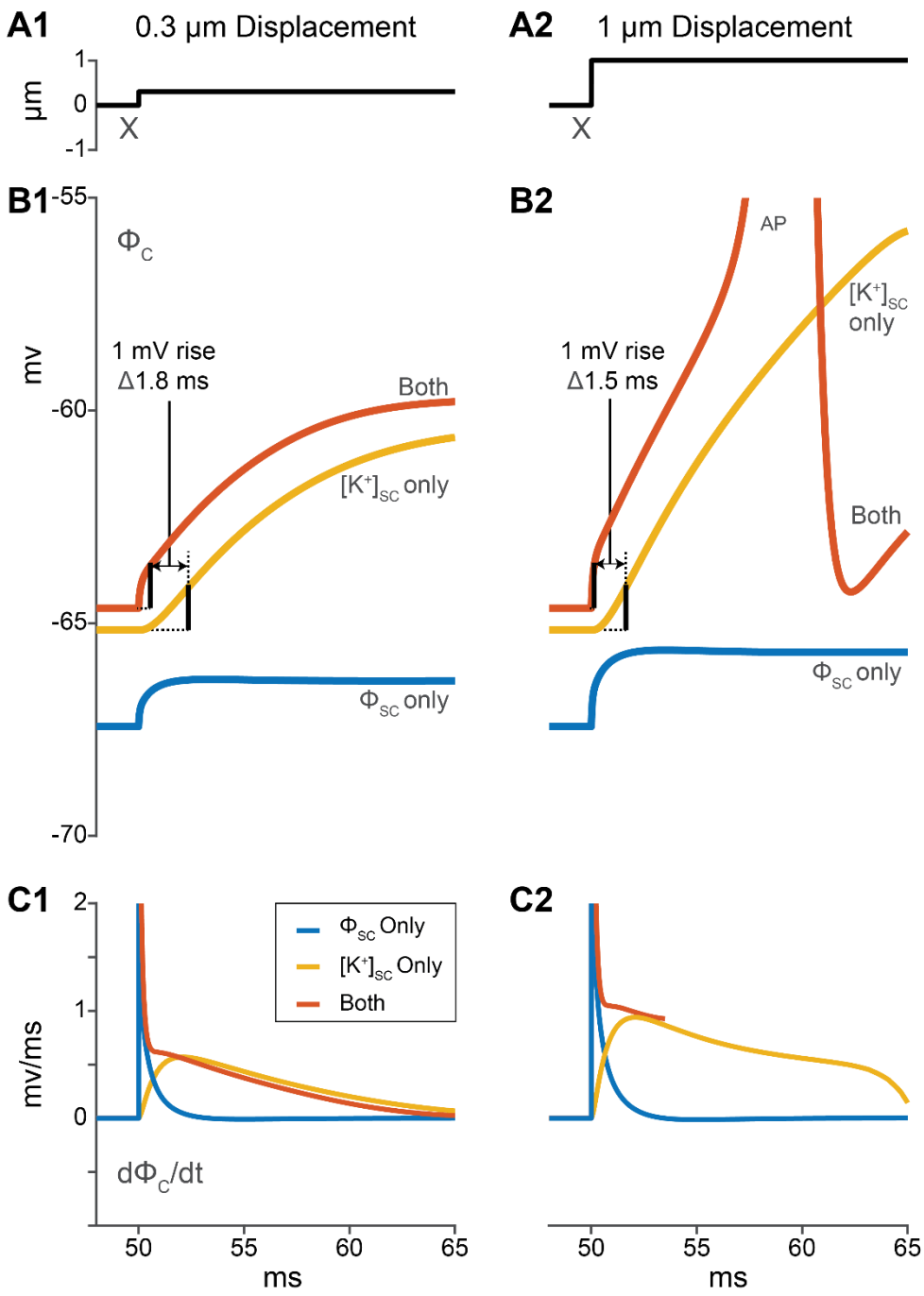

Fig. 4 – ϕ_{SC} and $[K^+]_{SC}$ are responsible for the fast and slow components of NQT respectively. Simulations for 2 bundle steps (**A1, A2**) with ϕ_{SC} modulation only (blue), with $[K^+]_{SC}$ modulation only (yellow) and with both enabled (dark orange).

B1,B2, Calyx potential (ϕ_C) rises faster when ϕ_{SC} is present, either alone or together with $[K^+]_{SC}$. The time to rise by 1 mV (dashed lines) clearly shows the lag in K^+ accumulation. Together, 'Both' changes trigger a calyx AP for the larger stimulus.

C1,C2, Rate of change of calyx potential highlights the kinetic differences in ϕ_{SC} and $[K^+]_{SC}$ changes. For clarity, the 'Both' curve (red) is truncated before the AP in **C2**.

bioRxiv preprint doi: https://doi.org/10.1101/2021.11.18.469197; this version posted April 29, 2022. The copyright holder for this preprint (which was not certified by peer review) is the author/funder. All rights reserved. No reuse allowed without permission.

The VHCC Model Captures the Frequency Response and Gain of NQT

Songer and Eatock (2013) recorded responses from calyces in the excised rat saccule to sinusoidal hair bundle stimulation between 2-100 Hz in order to capture the frequency filtering characteristics relevant to natural head motions (Cullen 2019). An example of NQT from these experiments is reproduced in **Fig. 5A.** In addition to measuring the frequency-following capacity of the NQT-induced changes in calyx potential (ϕ_C), these data showed that for large bundle displacements NQT alone (without quantal transmission) can trigger action potentials in the afferent. Here we show the VHCC model's ability to reproduce these salient features of the experimental data and use the model to illustrate the roles of $[K^+]_{SC}$ and ϕ_{SC} in shaping the calyx response (**Fig. 5**).

The model captures NQT-driven firing in response to sinusoidal stimulus. The model produced calyx potentials that are consistent with whole-cell recordings from a calyx in the central striolar zone of the rat saccular epithelium (**Fig. 5A**), including spikes for large stimuli. In both data and model, the calyx was most likely to spike for stimulus frequencies between 10 and 50 Hz.

Resistive currents dominate capacitive currents during bundle stimulation. The VHCC model enables us to track the contributions of capacitive and resistive currents to NQT as a function of frequency (**SI Eqs. S3-5, S8-13**). In **Fig. 5B** and **5C** a small stimulus ($\pm$0.3 µm) was used to avoid triggering APs and better reveal the underlying changes in hair cell current and postsynaptic potentials (ϕ_C). The model predicts resistive currents ($I_{H,R}$) are much larger than capacitive current ($I_{H,C}$) flowing from the type I hair cell (**Fig. 5B**, note the different y-axis limits). The capacitive current does increase with frequency, as expected, and can noticeably affect NQT during large voltage step stimuli (discussed later in Figure 6).

Changes in both ϕ_{SC} and $[K^+]_{SC}$ are required to explain the phase of the ϕ_C response to sinusoidal stimuli. We examined the contribution of ϕ_{SC} and $[K^+]_{SC}$ to the phase of ϕ_H (**Fig. 5C**) and ϕ_C (**Fig. 5E**) as a function of frequency. A positive phase indicates that the maximal response of ϕ_H or ϕ_C is achieved before the maximal bundle displacement and is indicative of a high-pass filtering process. As shown, ϕ_{SC} contributes to a positive phase response in ϕ_H at frequencies below 32 Hz. For ϕ_H, at lower frequencies, the positive phase arises from $g_{K,L}$ activation (for kinetics, see **SI Table S6**): during the depolarizing half cycle, an appreciable increase in $g_{K,L}$ (>10% at 2 Hz) produces an increasing outward current that truncates the rise in ϕ_H before the peak of the bundle displacement. Likewise, for ϕ_C the positive phase at lower frequencies arises from activation of K_{LV} channels within the calyx and fiber. The ϕ_C response was nearly

bioRxiv preprint doi: https://doi.org/10.1101/2021.11.18.469197; this version posted April 29, 2022. The copyright holder for this preprint (which was not certified by peer review) is the author/funder. All rights reserved. No reuse allowed without permission.

flat with frequency for the ϕ_{SC}-only condition but showed strong low-pass filtering for the $[K^+]_{SC}$-only component.

The low-pass behavior of [K$^+$] modulation can be explained by the time course of K$^+$ accumulation or depletion in the cleft (see **SI Eq. S3**). The influence of this effect is relatively slow because more ions are needed to change ion concentrations and chemical potentials than to change electrical potential. In contrast, modulation of ϕ_{SC} instantaneously affects voltage across both pre- and post-synaptic membranes, altering both capacitive currents and resistive (ionic) currents through open channels. This explains the short response latency at the onset of a step stimulus (**Fig. 4B**) and the ϕ_C phase response to sinusoidal stimuli. The ϕ_{SC} component is required to closely approximate the phase of experimental data above 5 Hz (**Fig. 5E**). This effect supports the evidence from step data (**Fig. 4**) that a stimulus-modulated electrical potential in the synaptic cleft speeds up NQT.

$[K^+]_{SC}$ dominates the gain of NQT but ϕ_{SC} slightly boosts gain at all frequencies. Next, we examined the normalized and actual gain of averaged peak ϕ_H (**Fig. D1,D2**) and ϕ_C (**Fig. F1,F2**) as a function of frequency. For ϕ_H, the $[K^+]_{SC}$ mechanism contributes to a positive gain that rolls off above ~20 Hz, while the ϕ_{SC} mechanism linearly increases with frequency. Interestingly, the ϕ_{SC} mechanism kicks in to noticeably boost the ϕ_H gain above ~30 Hz. For ϕ_C, the gain at low frequencies is larger for the $[K^+]_{SC}$ component than for the ϕ_{SC} component (**Fig. 5F2**). The model also shows that the $[K^+]$ modulation mechanism amplifies the calyx potential response at all frequencies but especially below 20 Hz. This effect is consistent with the increasing size of the $[K^+]_{SC}$ component relative to the ϕ_{SC} component with time during a displacement step (**Fig. 4B1,B2)**. The ϕ_{SC} component is approximately constant with frequency, and the model predicts will boost the high frequency gain (**Fig. 5F1).** However, the experimental ϕ_C gain (green) has a higher corner frequency (66 Hz) than the model output (36 Hz) which may reflect differences in afferent fiber properties in the model and specific experiments.

bioRxiv preprint doi: https://doi.org/10.1101/2021.11.18.469197; this version posted April 29, 2022. The copyright holder for this preprint (which was not certified by peer review) is the author/funder. All rights reserved. No reuse allowed without permission.

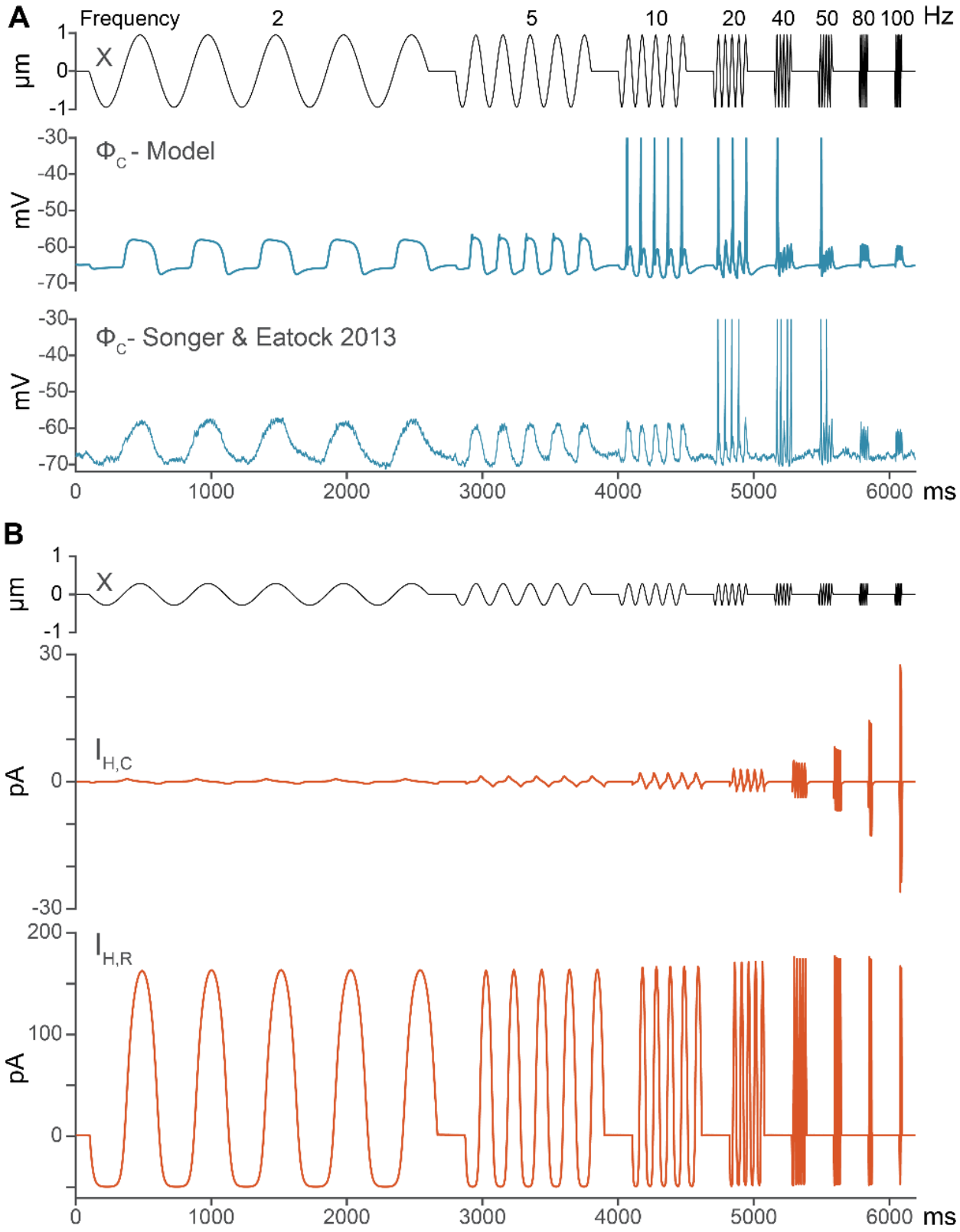

bioRxiv preprint doi: https://doi.org/10.1101/2021.11.18.469197; this version posted April 29, 2022. The copyright holder for this preprint (which was not certified by peer review) is the author/funder. All rights reserved. No reuse allowed without permission.

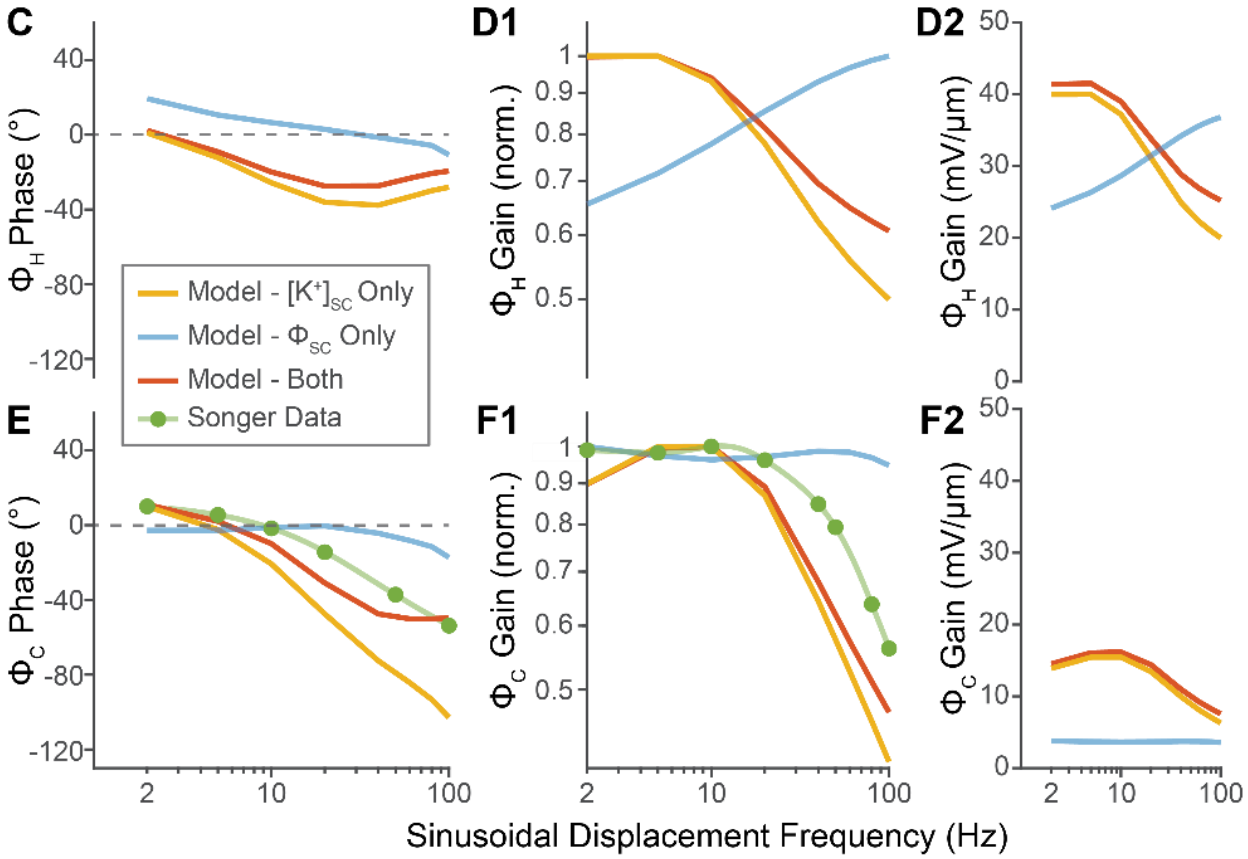

Fig. 5 – Resistive currents from the hair cell drive changes in ϕ_{SC} and $[K^+]_{SC}$ to shape the phase and gain of the transmitted signal (ϕ_C).

A, Modelled ϕ_C response and whole-cell current clamp recording of ϕ_C from rat saccular calyx (Songer and Eatock 2013, their Fig. 5B) during ±1 µm sinusoidal bundle displacement.

B-F, Model outputs for ±0.3 µm bundle displacement analyzed into ϕ_{SC} modulation-only component (*blue*), $[K^+]_{SC}$ modulation-only component (*yellow*) and *Both* together (*dark orange*).

B, Capacitive ($I_{H,C}$) and resistive ($I_{H,R}$) currents from the hair cell. $I_{H,R}$ is the primary contributor to changes in the synaptic cleft.

C-F, Bode plots showing phase (**C, E)**, normalized gain (**D1, F1)** and gain (**D2, F2**) of ϕ_H *and* ϕ_C relative to X**.**

E, $[K^+]_{SC}$ component (yellow) falls off much more steeply and with lower corner frequency than ϕ_{SC} component (blue). Combining them (dark orange) better matches experimental data (green, from Songer and Eatock 2013, their Fig. 5C).

F1,F2, $[K^+]_{SC}$ modulation dominates the gain of NQT between 2-100 Hz. Allowing ϕ_{SC} to also change (dark orange) slightly increases gain at higher frequencies (yellow, **F1**). ϕ_{SC} provides a small constant gain across a wide frequency band (**F2**).

bioRxiv preprint doi: https://doi.org/10.1101/2021.11.18.469197; this version posted April 29, 2022. The copyright holder for this preprint (which was not certified by peer review) is the author/funder. All rights reserved. No reuse allowed without permission.

Paired Voltage Clamp Recordings from Hair Cell and Calyx Provide Evidence of Changes in Synaptic Cleft Potential

We have previously speculated that NQT involves the flow of K^+ through a large number of $g_{K,L}$ channels that are open at typical hair cell resting potentials (Eatock 2018). In this condition, receptor potentials instantaneously change K^+ current flowing into the synaptic cleft, bypassing the time—on the order of 1-100 ms—required to activate voltage-gated channels from the closed conformation. Experiments by Contini et al. (2020), involving paired voltage-clamp recordings of whole-cell currents from turtle type I hair cells and postsynaptic calyces, address this hypothesis. In these experiments, the hair cell was stepped to +20 mV from either -100 mV or -70 mV, while the calyx was held at either –100 mV or -70 mV, and fast inward calyx currents were recorded (**Fig. 6A1,A2**, respectively). Contini et al. (2020) attribute these currents to 'resistive coupling' through pre-synaptic and post-synaptic ion channels open at the holding potential immediately prior to the voltage step. However, the driving forces underlying the recorded currents were unclear. Additionally, despite similar time courses and temporal proximity to the voltage step, one of the fast post-synaptic currents (**Fig. 6A1**) was thought to be an artefact. Here we show with the VHCC model that the fast post-synaptic currents at the two different holding potentials are both driven by changes in ϕ_{SC}, the electrical potential in the synaptic cleft.

The VHCC model was applied to analyze the experimental data with either the $[K^+]_{SC}$-only condition or the $[K^+]_{SC}$ *and* ϕ_{SC} ('Both') condition, described earlier. The fast post-synaptic currents only occurred in the 'Both' condition (**Fig. 6B1,B2**), illustrating that changes in ϕ_{SC} were the primary driving force and that the currents cannot be explained solely by changes in E_K. Under the 'Both' condition, we first examined the model's output for a calyx and hair cell holding potential of –100 mV (**Fig. 6, Left Column**), to compare with results from Contini et al. (2017, 2020). At this holding potential, $g_{K,L}$ and K_V7 channels were mostly closed and carried very little current prior to the voltage step. As ϕ_H is depolarized to +20 mV, ϕ_{SC} (**Fig. 6C1**) is primarily shaped by capacitive currents across the basolateral hair cell membrane ($I_{H,C}$) which precede $g_{K,L}$ activation (**Fig. 6D1,E1**). This variation in ϕ_{SC} alters V_{CIF}, shapes currents through the calyx inner face membrane (**Fig. 6B1, asterisk**), mostly via HCN2 channels (**Fig. 6E1**), and explains the current thought to be an artefact by Contini et al. 2020 (**Fig. 6A1, asterisk**). We identify these currents as evidence for changes in ϕ_{SC}, in response to depolarization of the hair cell.

We then examined the model's output for a calyx and hair cell holding potential –70 mV (**Fig. 6, Right Column**). At this holding potential, $g_{K,L}$ and K_V7 channels were significantly open prior to the voltage step. As ϕ_H is depolarized to +20 mV, ϕ_{SC} (**Fig. 6C2**) is primarily shaped by resistive currents through the

bioRxiv preprint doi: https://doi.org/10.1101/2021.11.18.469197; this version posted April 29, 2022. The copyright holder for this preprint (which was not certified by peer review) is the author/funder. All rights reserved. No reuse allowed without permission.

basolateral hair cell membrane ($I_{H,R}$), mostly via $g_{K,L}$ (**Fig. 6D2,E2**). This hyperpolarizes V_{CIF} (**Fig. 6B2**) and increases the inward driving force for currents through the calyx inner face, principally through K_V7 channels rather than HCN channels (**Fig. 6E2**). This results in a distinctive and fast current (double asterisks) of similar time course (albeit increased amplitude) to that seen by Contini et al. (2020) (compare **Fig. 6A2** and **6B2**). The difference in amplitude may reflect differences in key channel properties (e.g., the voltage dependence and size of $g_{K,L}$) and calyx geometry between the model parameters (based on data from mice and rats) and this particular experimental data (from turtles).

Under both experimental conditions (**Fig. 6A1,A2**) it is apparent that the recorded currents have a fast (asterisk and double asterisks) and a slow component. These components are consistent with the existence of two driving forces with different time courses — ϕ_{SC} and E_K. We note that ϕ_{SC} (**Fig. 6C1,C2**) follows the general shape of $\frac{d(\phi_H)}{dt}$ when capacitive currents dominate (at -100 mV holding condition) or ϕ_H when resistive currents from the hair cell dominate, which is the case near the holding potential of -70 mV (**Fig. 6D2, Fig. 5D**) and closer to reported hair cell resting potentials (~–80 to –60 mV, see **SI Table S4** for references). Comparison of the two different experimental conditions also demonstrates that open $g_{K,L}$ channels (**Fig. 6E2**) are responsible for the rapid and sustained transmission of the hair cell receptor potential to the calyx through changes in cleft potential and post-synaptic currents (**Fig. 6B2,C2**). These results show the importance for NQT of the unusual properties of $g_{K,L}$: together the large magnitude and the unusually negative half-activation voltage ensure that many channels are open near the hair cell resting potential and poised to respond to incoming stimuli.

bioRxiv preprint doi: https://doi.org/10.1101/2021.11.18.469197; this version posted April 29, 2022. The copyright holder for this preprint (which was not certified by peer review) is the author/funder. All rights reserved. No reuse allowed without permission.

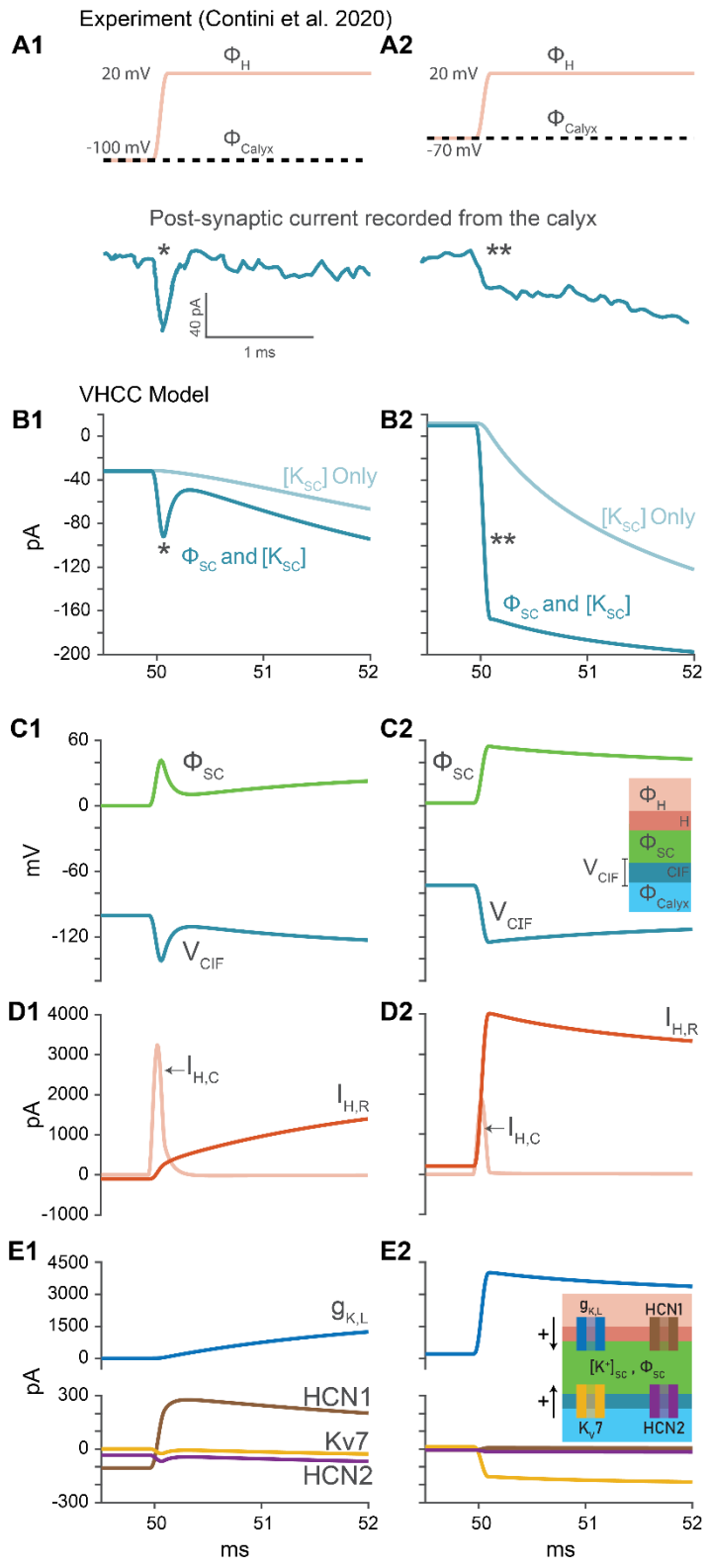

Fig. 6 – Changes in synaptic cleft potential ϕ_{SC} explain the shape of fast post-synaptic currents in paired voltage recordings.

A1,A2, Voltage protocols and currents from experiment. Calyx Potential (ϕ_C) held at -100 mV. Hair cell potential stepped at 50 ms from holding potential of -100 mV to 20 mV (**A1**). Calyx Potential (ϕ_{Calyx}) held at -70 mV. Hair cell potential stepped at 50 ms from holding potential of -70 mV to 20 mV (**A2**). Currents reproduced from Contini et al. (2020, their figure 10).

B1,B2, Resistive post-synaptic current through the calyx inner face membrane, $I_{CIF,R}$. Note that fast currents (* and **) do not occur in the $[K]_{SC}$-only case (faded blue).

C, Electrical potential in the synaptic cleft (ϕ_{SC}) and voltage across the calyx inner face (V_{CIF}) membrane. **C1,** The cleft potential is primarily shaped by capacitive currents from the hair cell ($I_{H,C}$, **D1**). **C2,** The cleft potential is primarily shaped by resistive currents from the hair cell ($I_{H,R}$, **D2**).

E, Whole cell currents through individual ion conductances. From the non-physiological -100 mV holding potential (A1), HCN1 hair-cell current is prominent, fast and sustained, because HCN channels are open at -100 mV (**E1**). Note that from -70 mV holding potential (A2), $g_{K,L}$ current is fast and sustained and K_V7 current (yellow) is the most prominent calyx current (**E2**). Currents through $g_{K,L}$ (E2) sustain the step in ϕ_{SC} following the voltage step in the hair cell. The slow decay reflects the change in driving force as K^+ accumulates in the cleft.

bioRxiv preprint doi: https://doi.org/10.1101/2021.11.18.469197; this version posted April 29, 2022. The copyright holder for this preprint (which was not certified by peer review) is the author/funder. All rights reserved. No reuse allowed without permission.

Nonquantal Transmission Depends on Calyx Morphology

The simulations we have presented are for a calyx shape typical of many calyces in the central and striolar zones of rodent vestibular epithelia (**Fig. 1**). However, calyces vary in their shape in different regions of amniote vestibular epithelia (Lysakowski et al. 2011), and shorter "proto-calyces" are reported to exist in fish and amphibians (Honrubia et al. 1989; Lanford and Popper 1996; Lysakowski and Goldberg 2004; Boyle et al. 2018). To address the effects of calyx geometry on the two components (ϕ_{SC} and $[K^+]_{SC}$) of NQT, we studied both the steady-state condition and the step response (**Fig. 7**) for different calyx heights, while retaining the same ion channel and transporter expression per unit area of membrane. As the calyx was truncated (**Fig. 7**, **'**1/2', '1/4') relative to the standard geometry (**Figs. 1** and **7**, **'**Calyx**'**), both ϕ_{SC} and $[K^+]_{SC}$ were closer to perilymph values (0 mV and 5 mM, respectively) at rest (**Fig. 7A,D**), had smaller responses to stimuli (**Fig. 7B,E**) and no spikes were initiated in the afferent fiber. However, the model does suggest that these truncated calyces, which resemble proto-calyces of anamniotes (assuming a similar distribution of ion channels) could accumulate K^+, and experience noticeable changes in E_K (**Fig. 7F**) that facilitate afferent depolarization. This effect on ϕ_C, at the onset of bundle stimulation, is small, ~2 mV (**Fig. 7C**). On the other hand, elongation of the calyx height by 2 μm (**Fig. 7, '**Ext**'**) increased ϕ_{SC} and $[K^+]_{SC}$ at rest, increased rate and magnitude of stimulus-evoked changes in ϕ_C, and reduced transmission latency (**Fig. 7C**). This greater height is found in the calyces of "dimorphic" afferents (Lysakowski et al. 2011), which have both calyx and bouton endings.

Fig. 7 shows that increasing calyx height (and thereby extending the synaptic cleft) increases the resting values of ϕ_{SC} and $[K^+]_{SC}$, depolarizes both hair cell and calyx potentials, opens more ion channels at rest, increases stimulus-evoked changes in both ϕ_{SC} and $[K^+]_{SC}$, increases the likelihood of post-synaptic spiking and reduces first-spike latency (**Fig. 7C**; the occurrence of a calyx spike is evident in the ϕ_{SC} traces for the standard and extended calyx). Simulations of calyx heights at finer intervals indicated that NQT-initiated spiking required a calyx height within 95% of the standard geometry (11.3 μm), suggesting the central calyx height may reflect a minimal value required for NQT-driven spiking. Interestingly, once this minimal length is achieved, further increases in calyx length have a significant effect on the magnitude and rate of NQT and time-to-spike in the calyx. In addition to an increase in the calyceal membrane, this reflects an increase in the extent of the synaptic cleft and the associated axial resistance and distance to perilymph.

bioRxiv preprint doi: https://doi.org/10.1101/2021.11.18.469197; this version posted April 29, 2022. The copyright holder for this preprint (which was not certified by peer review) is the author/funder. All rights reserved. No reuse allowed without permission.

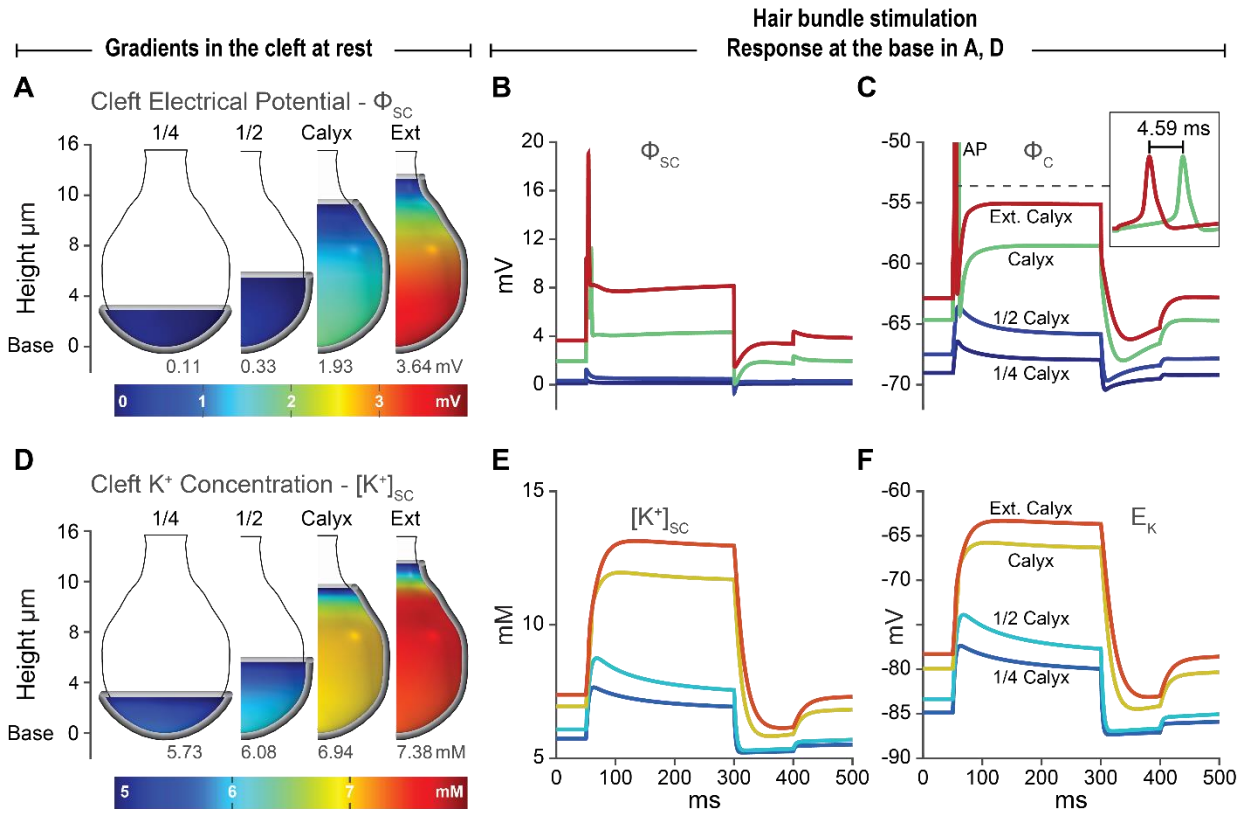

Fig. 7 – Magnitude and speed of nonquantal transmission increase with calyx height.
A, D, The 3D visualizations represent a shell the width of the cleft space resting between the hair cell and calyx. Silver edges delineate calyces of different heights. Spatial gradients of ϕ_{SC} and $[K^+]_{SC}$ are visible within these regions. The outer surface of the hair cell above the calyx is exposed to perilymph (ϕ = 0 mV, ground and [K⁺] = 5 mM). Values at the base of the synapse are shown above the color bars. **B,C,E,F,** Changes in ϕ_{SC}, $\phi_{C,}$ $[K^+]_{SC}$ and E_K increase with calyx height. Curve colors correspond to those at the base of each calyx in A and D at steady state.

A, The spatial distribution of ϕ_{SC} at rest as a function of calyx height.
B, ϕ_{SC} at the base of the synapse over the course of step bundle displacement (same as in Fig. 2A).
C, Changes in ϕ_C (the transmitted signal). The inset demonstrates the reduction in time to spike as calyx height is increased by 2 μm from 11.3 to 13.3 μm.
D, The spatial distribution of $[K^+]_{SC}$ at rest.
E, $[K^+]_{SC}$ at the base of the synapse over the course of step bundle displacement.
F, E_K values corresponding to changes in $[K^+]_{SC}$. Compare with ϕ_{SC} (**B**).

bioRxiv preprint doi: https://doi.org/10.1101/2021.11.18.469197; this version posted April 29, 2022. The copyright holder for this preprint (which was not certified by peer review) is the author/funder. All rights reserved. No reuse allowed without permission.

Discussion

We have constructed a biophysical model that incorporates ultrastructural data on the geometry of the VHCC synapse, immunocytochemical data on the expression of ion channels and transporters and electrophysiological data on kinetics of ion channels. Our goal was to understand how currents and driving forces interact to accomplish NQT at the unique VHCC synapse, which is characterized by its extensive and unfenestrated synaptic cleft, and the many low-voltage-activated potassium (K_{LV}) channels which populate the pre- and post-synaptic membranes. The model enables the prediction of experimentally inaccessible parameters, including potassium concentration $[K^+]_{SC}$ and electrical potential ϕ_{SC} in the synaptic cleft. The model also enables us to track dynamic changes in these parameters in response to hair bundle deflection and paired voltage clamp conditions. These capabilities have produced results which explain experimental recordings of both fast (Songer and Eatock 2013; Contini et al. 2020) and slow (Highstein et al. 2014; Contini et al. 2017) NQT. In the process, we were able to identify three overlooked features in existing experimental recordings which support the existence of an electrical potential in the synaptic cleft and its role in NQT as predicted by the model: the frequency dependence of the phase of NQT (Songer and Eatock 2013); the fast retrograde events in hair cell potential during retrograde transmission of post-synaptic spikes (Contini et al. 2017); and the shape of fast post-synaptic currents (Contini et al. 2020).

The VHCC model permits a clear description of the sequence of biophysical events that give rise to NQT, summarized in **Fig. 8** and shown in **Figs. 2,3**. Modulation of hair cell potential immediately changes the synaptic cleft potential ϕ_{SC} and more gradually changes the potassium potential E_K. Both are accomplished by change in a large K^+ current through the non-inactivating, low-voltage-activated potassium conductance, $g_{K,L}$, on the hair cell basolateral membrane. The properties of $g_{K,L}$ suit its role in NQT. First, $g_{K,L}$ is >50% open at the hair cell resting potential, allowing the receptor potential to immediately alter membrane current and thereby ϕ_{SC}. Second, $g_{K,L}$ is non-inactivating, ensuring that significant K^+ will accumulate in the cleft during sustained or low-frequency hair cell stimulation. The changes in cleft electrical and K^+ potentials alter the driving forces of currents across the calyx inner face. The calyx inner face contains a large number of different low-voltage-activated channels (Kv7), which are also non-inactivating and significantly open at rest (~30%). Upon stimulation, increases in ϕ_{SC} and $[K^+]_{SC}$ reduce the outward Kv7 current and depolarize the calyx. In short, the presence of open K_{LV} channels in the pre- and post-synaptic membranes enables NQT as previously proposed (Eatock 2018; Spaiardi et al.

bioRxiv preprint doi: https://doi.org/10.1101/2021.11.18.469197; this version posted April 29, 2022. The copyright holder for this preprint (which was not certified by peer review) is the author/funder. All rights reserved. No reuse allowed without permission.

2020). The VHCC model clarifies the role of ϕ_{SC} and E_K as driving forces for currents through all channels facing the synaptic cleft.

The hypothesis that currents flow through open channels on either side of the membrane was tested experimentally and qualitatively presented as 'resistive coupling' between presynaptic $g_{K,L}$ and postsynaptic HCN channels (Contini et al. 2020). Fast post-synaptic currents were presented as evidence for resistive coupling but the driving forces that shaped these currents were not understood, and some were thought to be artefacts. Using the VHCC model, we have demonstrated that changes in cleft electrical potential, shaped by capacitive and resistive currents from the hair cell, underlie these fast post-synaptic currents.

At the calyx of Held, a different large synapse important for auditory processing (Borst and Soria van Hoeve 2012), analysis of ephaptic coupling (Sierksma and Borst 2021) suggested that although pre-synaptic capacitive and resistive currents occur, the fenestrated morphology of the calyx of Held serves to mitigate synaptic cleft potentials to ensure presynaptic calcium channels sense the full presynaptic action potential and rapidly actuate neurotransmitter release. In contrast, what naturally emerges from the VHCC model is that the unfenestrated morphology of the VHCC synapse is specialized to actively use cleft $[K^+]_{SC}$ and ϕ_{SC} as complementary mechanisms that mediate NQT and benefit signal transmission between the sensory hair cell and the afferent neuron. The slower changes in $[K^+]_{SC}$ increase the gain of NQT for slow or sustained hair bundle deflections, but do not alone explain the observed phase response. The near-instantaneous change in ϕ_{SC} enables the calyx to closely follow changes in hair cell potential and explains the short latency and phase characteristics of NQT observed experimentally (Songer and Eatock 2013; Contini et al. 2020). Ultimately NQT also enables afferent neurons to follow the stimulus up to relatively high frequencies. The calyx geometry is essential for both fast and slow NQT; as calyx height increases the efficacy of both mechanisms, ϕ_{SC} and $[K^+]_{SC}$, increases and transmission latency decreases.

These findings explain the exceptional speed of neurotransmission between type I hair cells and vestibular afferents, which is even faster than the quantal transmission between cochlear hair cells and afferents (McCue and Guinan 1994). At its fastest, quantal transmission imposes a 0.4-0.6-ms delay (Lisman et al. 2007), reflecting the time required for multiple steps from the opening of presynaptic voltage-gated calcium channels to the opening of postsynaptic neurotransmitter-gated receptor channels. For fast vestibular reflexes, with latencies as short as 5 ms between head motion and motor response (Huterer and Cullen 2002), overcoming quantal transmission delay and providing an additional mode of

bioRxiv preprint doi: https://doi.org/10.1101/2021.11.18.469197; this version posted April 29, 2022. The copyright holder for this preprint (which was not certified by peer review) is the author/funder. All rights reserved. No reuse allowed without permission.

communication through NQT at the first synapse in the pathway is a significant advantage. Our results indicate that robust NQT, enabled by the evolution of the full calyx, substantially reduces the latency and advances the phase of vestibular signals that drive neural circuits controlling gaze, balance, and orientation.

In conclusion, the VHCC model provides a quantitative description of NQT and describes two parallel mechanisms of NQT: changes in the cleft electrical potential and changes in the potassium potential. It also delineates the roles of specific ion channels and calyx geometry in NQT. Here we have focused on a simple calyx from central or striolar zones of vestibular epithelia; the model can be extended to explore the functional effects of other afferent terminal forms, such as the complex calyces that enwrap multiple type I hair cells and the elaborate dimorphic terminal arbors that include calyces and boutons (reviewed in Goldberg 2000; Eatock and Songer 2011).

bioRxiv preprint doi: https://doi.org/10.1101/2021.11.18.469197; this version posted April 29, 2022. The copyright holder for this preprint (which was not certified by peer review) is the author/funder. All rights reserved. No reuse allowed without permission.

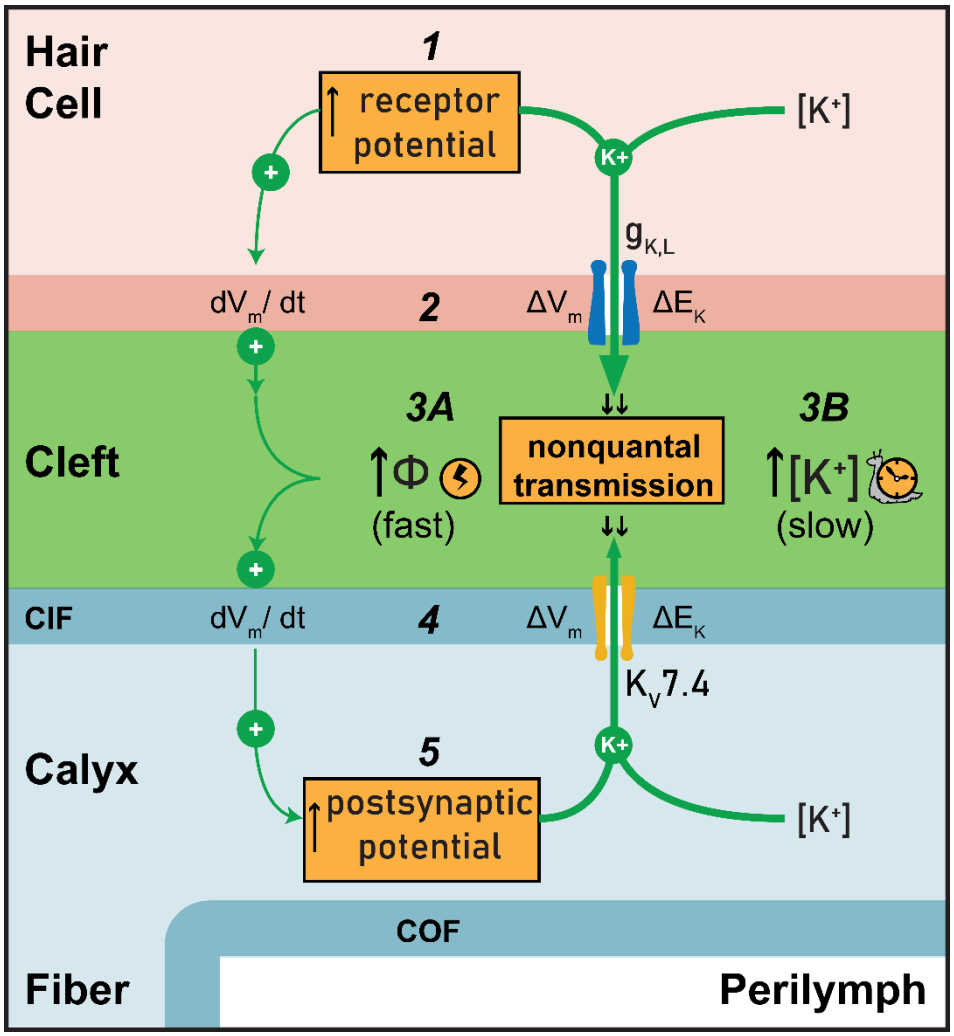

Fig. 8 – Nonquantal Transmission

1. Depolarizing receptor potential due to positive bundle deflection.
2. Change in hair cell membrane voltage drives capacitive currents (left pathway) and *increases* outward resistive current through $g_{K,L}$ (right pathway).
3. Changes in the synaptic cleft
   a. Fast rise in potential in the synaptic cleft, ϕ_{SC}
   b. Gradual rise in cleft potassium concentration $[K^+]_{SC}$
4. Changes in ϕ_{SC} and $[K^+]_{SC}$ alter membrane voltage and E_K respectively across the calyx inner face. This drives capacitive currents (left pathway) and *decreases* outward resistive current through $K_V7.4$ (right pathway). During bundle stimulation, resistive currents in steps 2,4 are much larger than capacitive currents.
5. The postsynaptic potential depolarizes (Calyx is depolarized). Note that the cleft compartmentalizes the calyx membrane into inner (CIF) and outer (COF) faces, with different trans-membrane voltages. The postsynaptic potential corresponds to that measured with respect to perilymph and across the calyx outer face.

bioRxiv preprint doi: https://doi.org/10.1101/2021.11.18.469197; this version posted April 29, 2022. The copyright holder for this preprint (which was not certified by peer review) is the author/funder. All rights reserved. No reuse allowed without permission.

Data Availability

The model was implemented in Comsol Multiphysics 5.6 software. Equations and data sources are available in **SI Computational Methods and Experimental Methods.** The Comsol file (.mph) containing the model will be publicly available on Github (https://github.com/acgsci/vestibularHairCellCalyxNQT).

Author Contributions:

RAE and RMR conceived and supervised the work. ACG expanded an initial model developed by IQ. ACG and IQ wrote COMSOL and Matlab code for model implementation. RAE and AL supervised the acquisition of data presented in the Supplement. The manuscript was written by ACG, RMR and RAE and revised and edited by all authors.

Acknowledgements

This study was supported by National Institutes of Health (R01 DC012347 and DC002290) and a seed grant from the RICE ENRICH program. We are grateful to Hannah Martin for stimulating discussions and Selina Baeza-Loya for providing activation and inactivation time constants of afferent voltage-gated sodium channels.

bioRxiv preprint doi: https://doi.org/10.1101/2021.11.18.469197; this version posted April 29, 2022. The copyright holder for this preprint (which was not certified by peer review) is the author/funder. All rights reserved. No reuse allowed without permission.

References

Bao H, **Wong WH**, **Goldberg JM**, **Eatock RA**. Voltage-gated calcium channel currents in type I and type II hair cells isolated from the rat crista. *J Neurophysiol* 90: 155–164, 2003.

Baumann SB, **Wozny DR**, **Kelly SK**, **Meno FM**. The electrical conductivity of human cerebrospinal fluid at body temperature. *IEEE Trans Biomed Eng* 44: 220–223, 1997.

Bezanilla F. Single sodium channels from the squid giant axon. *Biophys J* 52: 1087–1090, 1987.

Borst JGG, **Soria van Hoeve J**. The calyx of Held synapse: from model synapse to auditory relay. *Annu Rev Physiol* 74: 199–224, 2012.

Boyle R, **Ehsanian R**, **Mofrad A**, **Popova Y**, **Varelas J**. Morphology of the utricular otolith organ in the toadfish, *Opsanus tau*. *J Comp Neurol* 526: 1571–1588, 2018.

Chabbert C, **Chambard JM**, **Sans A**, **Desmadryl G**. Three types of depolarization-activated potassium currents in acutely isolated mouse vestibular neurons. *J Neurophysiol* 85: 1017–1026, 2001.

Chen JWY. The properties and functions of a low-voltage activated potassium ion current in type I hair cells of rat semicircular canal organs. *ProQuest Dissertations and Theses,* University of Rochester, 1995.

Chen JWY, **Eatock RA**. Major potassium conductance in type I hair cells from rat semicircular canals: characterization and modulation by nitric oxide. *J Neurophysiol* 84: 139–151, 2000.

Chiang C, **Shivacharan RS**, **Wei X**, **Gonzalez-Reyes LE**, **Durand DM**. Slow periodic activity in the longitudinal hippocampal slice can self-propagate non-synaptically by a mechanism consistent with ephaptic coupling. *J Physiol* 597: 249–269, 2019.

Colebatch JG, **Rosengren SM**. Investigating short latency subcortical vestibular projections in humans: what have we learned? *J Neurophysiol* 122: 2000–2015, 2019.

Contini D, **Holstein GR**, **Art JJ**. Synaptic cleft microenvironment influences potassium permeation and synaptic transmission in hair cells surrounded by calyx afferents in the turtle. *J Physiol* 598: 853–889, 2020.

Contini D, **Price SD**, **Art JJ**. Accumulation of K^+ in the synaptic cleft modulates activity by influencing both vestibular hair cell and calyx afferent in the turtle. *J Physiol* 595: 777–803, 2017.

Contini D, **Zampini V**, **Tavazzani E**, **Magistretti J**, **Russo G**, **Prigioni I**, **Masetto S**. Intercellular K^+ accumulation depolarizes type I vestibular hair cells and their associated afferent nerve calyx. *Neuroscience* 227: 232–246, 2012.

Corey DP, **Akyuz N**, **Holt JR**. Function and dysfunction of TMC channels in inner ear hair cells. *Cold Spring Harb Perspect Med* 9: a033506, 2019.

Corns LF, **Johnson SL**, **Kros CJ**, **Marcotti W**. Calcium entry into stereocilia drives adaptation of the mechanoelectrical transducer current of mammalian cochlear hair cells. *Proc Natl Acad Sci USA* 111: 14918–14923, 2014.

bioRxiv preprint doi: https://doi.org/10.1101/2021.11.18.469197; this version posted April 29, 2022. The copyright holder for this preprint (which was not certified by peer review) is the author/funder. All rights reserved. No reuse allowed without permission.

Correia MJ, **Lang DG**. An electrophysiological comparison of solitary type I and type II vestibular hair cells. *Neurosci Lett* 116: 106–111, 1990.

Crambert G, **Hasler U**, **Beggah AT**, **Yu C**, **Modyanov NN**, **Horisberger J-D**, **Lelièvre L**, **Geering K**. Transport and pharmacological properties of nine different human Na,K-ATPase isozymes. *J Biol Chem* 275: 1976–1986, 2000.

Cullen KE. Vestibular processing during natural self-motion: implications for perception and action. *Nat Rev Neurosci* 20: 346–363, 2019.

Curthoys IS, **Grant JW**, **Pastras CJ**, **Brown DJ**, **Burgess AM**, **Brichta AM**, **Lim R**. A review of mechanical and synaptic processes in otolith transduction of sound and vibration for clinical VEMP testing. *J Neurophysiol* 122: 259–276, 2019.

Curtis HJ, **Cole KS**. Transverse electric impedance of the squid giant axon. *J Gen Physiol* 21: 757–765, 1938.

Dalet A, **Bonsacquet J**, **Gaboyard-Niay S**, **Calin-Jageman I**, **Chidavaenzi RL**, **Venteo S**, **Desmadryl G**, **Goldberg JM**, **Lysakowski A**, **Chabbert C**. Glutamate transporters EAAT4 and EAAT5 are expressed in vestibular hair cells and calyx endings. *PLoS ONE* 7: e46261, 2012.

Desai SS, **Zeh C**, **Lysakowski A**. Comparative morphology of rodent vestibular periphery. I. Saccular and utricular maculae. *J Neurophysiol* 93: 251–266, 2005.

Eatock RA. Specializations for fast signaling in the amniote vestibular inner ear. *Integr Comp Biol* 58: 341–350, 2018.

Eatock RA, **Songer JE**. Vestibular hair cells and afferents: Two channels for head motion signals. *Annu Rev Neurosci* 34: 501–534, 2011.

Faber DS, **Pereda AE**. Two forms of electrical transmission between neurons. *Front Mol Neurosci* 11: 427, 2018.

Freeman SA, **Desmazières A**, **Fricker D**, **Lubetzki C**, **Sol-Foulon N**. Mechanisms of sodium channel clustering and its influence on axonal impulse conduction. *Cell Mol Life Sci* 73: 723–735, 2016.

Geddes LA, **Baker LE**. The specific resistance of biological material--a compendium of data for the biomedical engineer and physiologist. *Med Biol Eng* 5: 271–293, 1967.

Gentet LJ, **Stuart GJ**, **Clements JD**. Direct measurement of specific membrane capacitance in neurons. *Biophys J* 79: 314–320, 2000.

Ginzberg RD. Freeze-fracture morphology of the vestibular hair cell-primary afferent synapse in the chick. *J Neurocytol* 13: 393–405, 1984.

Goldberg JM. Theoretical analysis of intercellular communication between the vestibular type I hair cell and its calyx ending. *J Neurophysiol* 76: 1942–1957, 1996.

bioRxiv preprint doi: https://doi.org/10.1101/2021.11.18.469197; this version posted April 29, 2022. The copyright holder for this preprint (which was not certified by peer review) is the author/funder. All rights reserved. No reuse allowed without permission.

Goldberg JM. Afferent diversity and the organization of central vestibular pathways. *Exp Brain Res* 130: 277–297, 2000.

Gourdie RG. The cardiac gap junction has discrete functions in electrotonic and ephaptic coupling. *Anat Rec* 302: 93–100, 2019.

Gulley RL, **Bagger-Sjöbäck D**. Freeze-fracture studies on the synapse between the type I hair cell and the calyceal terminal in the guinea-pig vestibular system. *J Neurocytol* 8: 591–603, 1979.

Han K-S, **Chen CH**, **Khan MM**, **Guo C**, **Regehr WG**. Climbing fiber synapses rapidly and transiently inhibit neighboring Purkinje cells via ephaptic coupling. *Nat Neurosci* 23: 1399–1409, 2020.

Han K-S, **Guo C**, **Chen CH**, **Witter L**, **Osorno T**, **Regehr WG**. Ephaptic coupling promotes synchronous firing of cerebellar purkinje cells. *Neuron* 100: 564-578.e3, 2018.

Highstein SM, **Holstein GR**, **Mann MA**, **Rabbitt RD**. Evidence that protons act as neurotransmitters at vestibular hair cell–calyx afferent synapses. *Proc Natl Acad Sci USA* 111: 5421–5426, 2014.

Hoffman LF, **Honrubia V**. Fiber diameter distributions in the chinchilla's ampullary nerves. *Hear Res* 172: 37–52, 2002.

Holt JC, **Chatlani S**, **Lysakowski A**, **Goldberg JM**. Quantal and nonquantal transmission in calyx-bearing fibers of the turtle posterior crista. *J Neurophysiol* 98: 1083–1101, 2007.

Holt JC, **Jordan PM**, **Lysakowski A**, **Shah A**, **Barsz K**, **Contini D**. Muscarinic acetylcholine receptors and M-currents underlie efferent-mediated slow excitation in calyx-bearing vestibular afferents. *J Neurosci* 37: 1873–1887, 2017.

Holt JR, **Corey DP**, **Eatock RA**. Mechanoelectrical transduction and adaptation in hair cells of the mouse utricle, a low-frequency vestibular organ. *J Neurosci* 17: 8739–8748, 1997.

Honrubia V, **Hoffman LF**, **Sitko S**, **Schwartz IR**. Anatomic and physiological correlates in bullfrog vestibular nerve. *J Neurophysiol* 61: 688–701, 1989.

Horwitz GC, **Risner-Janiczek JR**, **Holt JR**. Mechanotransduction and hyperpolarization-activated currents contribute to spontaneous activity in mouse vestibular ganglion neurons. *J Gen Physiol* 143: 481–497, 2014.

Horwitz GC, **Risner-Janiczek JR**, **Jones SM**, **Holt JR**. HCN channels expressed in the inner ear are necessary for normal balance function. *J Neurosci* 31: 16814–16825, 2011.

Hurley KM, **Gaboyard S**, **Zhong M**, **Price SD**, **Wooltorton JRA**, **Lysakowski A**, **Eatock RA**. M-like K^+ currents in type I hair cells and calyx afferent endings of the developing rat utricle. *J Neurosci* 26: 10253–10269, 2006.

Huterer M, **Cullen KE**. Vestibuloocular reflex dynamics during high-frequency and high-acceleration rotations of the head on body in rhesus monkey. *J Neurophysiol* 88: 13–28, 2002.

bioRxiv preprint doi: https://doi.org/10.1101/2021.11.18.469197; this version posted April 29, 2022. The copyright holder for this preprint (which was not certified by peer review) is the author/funder. All rights reserved. No reuse allowed without permission.

Jaisser F, **Jaunin P**, **Geering K**, **Rossier BC**, **Horisberger JD**. Modulation of the Na,K-pump function by beta subunit isoforms. *J Gen Physiol* 103: 605–623, 1994.

Jefferys JG. Nonsynaptic modulation of neuronal activity in the brain: electric currents and extracellular ions. *Physiol Rev* 75: 689–723, 1995.

Kalluri R, **Xue J**, **Eatock RA**. Ion channels set spike timing regularity of mammalian vestibular afferent neurons. *J Neurophysiol* 104: 2034–2051, 2010.

Kay AR, **Sugimori M**, **Llinás R**. Kinetic and stochastic properties of a persistent sodium current in mature guinea pig cerebellar Purkinje cells. *J Neurophysiol* 80: 1167–1179, 1998.

Köppl C, **Wilms V**, **Russell IJ**, **Nothwang HG**. Evolution of endolymph secretion and endolymphatic potential generation in the vertebrate inner ear. *Brain Behav Evol* 92: 1–31, 2018.

Lanford PJ, **Popper AN**. Novel afferent terminal structure in the crista ampullaris of the goldfish, carassius auratus. *J Comp Neurol* 366: 572–579, 1996.

Lee C-H, **MacKinnon R**. Structures of the human HCN1 hyperpolarization-activated channel. *Cell* 168: 111-120.e11, 2017.

Li Y, **Liu H**, **Zhao X**, **He DZ**. Endolymphatic potential measured from developing and adult mouse inner ear. *Front Cell Neurosci* 14: 584928–584928, 2020.

Lide DR, editor. "Ionic conductivity and diffusion at infinite dilution". In: *CRC Handbook of Chemistry and Physics, Internet Version 2005*, <http://www.hbcpnetbase.com>, Boca Raton, FL: CRC Press, 2005.

Lim R, **Kindig AE**, **Donne SW**, **Callister RJ**, **Brichta AM**. Potassium accumulation between type I hair cells and calyx terminals in mouse crista. *Exp Brain Res* 210: 607–621, 2011.

Lisman JE, **Raghavachari S**, **Tsien RW**. The sequence of events that underlie quantal transmission at central glutamatergic synapses. *Nat Rev Neurosci* 8: 597–609, 2007.

Liu X-P, **Wooltorton JRA**, **Gaboyard-Niay S**, **Yang F-C**, **Lysakowski A**, **Eatock RA**. Sodium channel diversity in the vestibular ganglion: Na_V 1.5, Na_V 1.8, and tetrodotoxin-sensitive currents. *J Neurophysiol* 115: 2536–2555, 2016.

Lysakowski A, **Gaboyard-Niay S**, **Calin-Jageman I**, **Chatlani S**, **Price SD**, **Eatock RA**. Molecular microdomains in a sensory terminal, the vestibular calyx ending. *J Neurosci* 31: 10101–10114, 2011.

Lysakowski A, **Goldberg JM**. A regional ultrastructural analysis of the cellular and synaptic architecture in the chinchilla cristae ampullares. *J Comp Neurol* 389: 419–443, 1997.

Lysakowski A, **Goldberg JM**. Morphophysiology of the vestibular periphery. In: *The Vestibular System*, Highstein SM, Fay RR, Popper AN, editors. Springer New York, pp. 57–152, 2004.

Lysakowski A, **Goldberg JM**. Ultrastructural analysis of the cristae ampullares in the squirrel monkey (Saimiri sciureus). *J Comp Neurol* 511: 47–64, 2008.

bioRxiv preprint doi: https://doi.org/10.1101/2021.11.18.469197; this version posted April 29, 2022. The copyright holder for this preprint (which was not certified by peer review) is the author/funder. All rights reserved. No reuse allowed without permission.

Marcoux AA, **Garneau AP**, **Frenette-Cotton R**, **Slimani S**, **Mac-Way F**, **Isenring P**. Molecular features and physiological roles of K^+ - Cl^- cotransporter 4 (KCC4). *Biochim Biophys Acta (BBA)* 1861: 3154–3166, 2017.

McCue M, **Guinan J**. Acoustically responsive fibers in the vestibular nerve of the cat. *J Neurosci* 14: 6058–6070, 1994.

Mercado A, **Song L**, **Vázquez N**, **Mount DB**, **Gamba G**. Functional comparison of the K^+-Cl^- cotransporters KCC1 and KCC4. *J Biol Chem* 275: 30326–30334, 2000.

Meredith FL, **Rennie KJ**. Zonal variations in K^+ currents in vestibular crista calyx terminals. *J Neurophysiol* 113: 264–276, 2015.

Meredith FL, **Rennie KJ**. Regional and developmental differences in Na^+ currents in vestibular primary afferent neurons. *Front Cell Neurosci* 12: 423, 2018.

Nicholson C, **Phillips JM**. Ion diffusion modified by tortuosity and volume fraction in the extracellular microenvironment of the rat cerebellum. *J Physiol* 321: 225–257, 1981.

Nielsen MS, **Nygaard Axelsen L**, **Sorgen PL**, **Verma V**, **Delmar M**, **Holstein-Rathlou N-H**. Gap junctions. In: *Comprehensive Physiology* 2: 1981-2035, 2012.

Rennie KJ, **Correia MJ**. Potassium currents in mammalian and avian isolated type I semicircular canal hair cells. *J Neurophysiol* 71: 317–329, 1994.

Rennie KJ, **Ricci AJ**, **Correia MJ**. Electrical filtering in gerbil isolated type I semicircular canal hair cells. *J Neurophysiol* 75: 2117–2123, 1996.

Ritchie JM, **Rogart RB**. Density of sodium channels in mammalian myelinated nerve fibers and nature of the axonal membrane under the myelin sheath. *Proc Natl Acad Sci USA* 74: 211–215, 1977.

Rüsch A, **Eatock RA**. A delayed rectifier conductance in type I hair cells of the mouse utricle. *J Neurophysiol* 76: 995–1004, 1996.

Sadeghi SG, **Pyott SJ**, **Yu Z**, **Glowatzki E**. Glutamatergic signaling at the vestibular hair cell calyx synapse. *J Neurosci* 34: 14536–14550, 2014.

Schuth O, **McLean WJ**, **Eatock RA**, **Pyott SJ**. Distribution of Na,K-ATPase α subunits in rat vestibular sensory epithelia. *J Assoc Res Otolaryngol* 15: 739–754, 2014.

Sierksma MC, **Borst JGG**. Using ephaptic coupling to estimate the synaptic cleft resistivity of the calyx of Held synapse. *PLoS Comput Biol* 17: e1009527, 2021.

Songer JE, **Eatock RA**. Tuning and timing in mammalian type I hair cells and calyceal synapses. *J Neurosci* 33: 3706–3724, 2013.

Soto E, **Vega R**, **Budelli R**. The receptor potential in type I and type II vestibular system hair cells: a model analysis. *Hear Res* 165: 35–47, 2002.

bioRxiv preprint doi: https://doi.org/10.1101/2021.11.18.469197; this version posted April 29, 2022. The copyright holder for this preprint (which was not certified by peer review) is the author/funder. All rights reserved. No reuse allowed without permission.

Spaiardi P, **Tavazzani E**, **Manca M**, **Milesi V**, **Russo G**, **Prigioni I**, **Marcotti W**, **Magistretti J**, **Masetto S**. An allosteric gating model recapitulates the biophysical properties of $I_{K,L}$ expressed in mouse vestibular type I hair cells: Allosteric gating of $I_{K,L}$. *J Physiol* 595: 6735–6750, 2017.

Spaiardi P, **Tavazzani E**, **Manca M**, **Russo G**, **Prigioni I**, **Biella G**, **Giunta R**, **Johnson SL**, **Marcotti W**, **Masetto S**. K^+ accumulation and clearance in the calyx synaptic cleft of type I mouse vestibular hair cells. *Neuroscience* 426: 69–86, 2020.

Stämpfli R. Saltatory conduction in nerve. *Physiol Rev* 34: 101–112, 1954.

Veeraraghavan R, **Poelzing S**, **Gourdie RG**. Intercellular electrical communication in the heart: A new, active role for the intercalated disk. *Cell Commun Adhes* 21: 161–167, 2014.

Ventura CM, **Kalluri R**. Enhanced activation of HCN channels reduces excitability and spike-timing regularity in maturing vestibular afferent neurons. *J Neurosci* 39: 1811–18, 2019.

Vroman R, **Klaassen LJ**, **Kamermans M**. Ephaptic communication in the vertebrate retina. *Front Hum Neurosci* 7: 612, 2013.

Wang K, **Zhao Y**, **Chen D**, **Fan B**, **Lu Y**, **Chen L**, **Long R**, **Wang J**, **Chen J**. Specific membrane capacitance, cytoplasm conductivity and instantaneous Young's modulus of single tumour cells. *Scientific Data* 4: 170015, 2017.

Warren TJ, **Van Hook MJ**, **Tranchina D**, **Thoreson WB**. Kinetics of inhibitory feedback from horizontal cells to photoreceptors: implications for an ephaptic mechanism. *J Neurosci* 36: 10075–10088, 2016.

Wersäll J. Studies on the structure and innervation of the sensory epithelium of the cristae ampulares in the guinea pig; a light and electron microscopic investigation. *Acta Otolaryngol Suppl* 126: 1–85, 1956.

Wong WH, **Hurley KM**, **Eatock RA**. Differences between the negatively activating potassium conductances of mammalian cochlear and vestibular hair cells. *J Assoc Res Otolaryngol* 5: 270–284, 2004.

Yamashita M, **Ohmori H**. Synaptic responses to mechanical stimulation in calyceal and bouton type vestibular afferents studied in an isolated preparation of semicircular canal ampullae of chicken. *Exp Brain Res* 80: 475–488, 1990.

Yamashita M, **Ohmori H**. Synaptic bodies and vesicles in the calix type synapse of chicken semicircular canal ampullae. *Neurosci Lett* 129: 43–46, 1991.

Zhou T, **Ming Y**, **Perry SF**, **Tatic-Lucic S**. Estimation of the physical properties of neurons and glial cells using dielectrophoresis crossover frequency. *J Biol Phys* 42: 571–586, 2016.

bioRxiv preprint doi: https://doi.org/10.1101/2021.11.18.469197; this version posted April 29, 2022. The copyright holder for this preprint (which was not certified by peer review) is the author/funder. All rights reserved. No reuse allowed without permission.

Supplementary Information

Computational Methods

Overview. The Vestibular Hair Cell-Calyx (VHCC) model incorporates information on synapse morphology, ion transporters and ion channels expressed in type I hair cells (channel types: transduction (MET), K_V, Ca_V, HCN; transporter: Na^+/K^+-ATPase), and in calyces and afferent fibers (channel types: K_V, Na_V, HCN; transporters: KCC, Na^+/K^+-ATPase) (see **Fig. 1** in main text). The dynamic behavior of the system is determined from measured or estimated channel open probabilities, time constants and whole-cell conductances, and from assumptions (which we describe) about the activity of ion transporters based on literature. We implemented the VHCC model with finite-element-analysis simulation software, using equations for K^+ and Na^+ electro-diffusion in the cleft, Hodgkin-Huxley-style equations to represent voltage-dependent ion flow through ion channels, and the cable equation for electrical propagation. For each simulation, steady-state conditions are established and followed by a step or sinusoidal deflection of the hair bundle or voltage step; outputs include the basal-to-apical gradients within the synaptic cleft for K^+, Na^+ and electrical potential, and voltage across the hair-cell-facing postsynaptic membrane of the calyx ("calyx inner face"), and in the hemi-node and first two full nodes of the distal branch of the bipolar vestibular afferent neuron. The distal branch connects the synaptic terminals on hair cells (in this case a single calyx) to the neuronal cell body in the vestibular ganglion; the remainder of the distal branch, the cell body and the central branch projecting to the brain are not included in the model. Negative currents represent the flow of cations into the compartment bearing the channel or transporter in its membrane. The hair cell is assumed to be equipotential based on its small overall size, compact form and low intracellular resistance. Details of model development are described below.

Model Geometry. The model was designed with the COMSOL Multiphysics 5.6 software package. We used a 2D axisymmetric finite element boundary to represent the hair cell, synaptic cleft, and afferent calyx and a 1D finite element line to represent the afferent fiber (**Fig. S1**). The 2D boundary used to represent the hair cell (H), synaptic cleft (SC), the calyx inner face (CIF) and calyx outer face (COF) is an interpolation curve generated from (R,Z) coordinates of the perimeter of a central-zone hair cell and calyx from the central zone of the sensory epithelium of a crista in an adult Long-Evans rat (shown in Fig. 2C of Lysakowski et al. 2011; similar calyces from the striolar zone of the rat utricle are shown in our **Fig. 1A**). The dimensions and interpolated points used to create the representative geometry in Comsol 5.6 are

bioRxiv preprint doi: https://doi.org/10.1101/2021.11.18.469197; this version posted April 29, 2022. The copyright holder for this preprint (which was not certified by peer review) is the author/funder. All rights reserved. No reuse allowed without permission.

shown in **Fig. S1.** HN, N and M indicate the hemi-node, nodes and myelinated sections (inter-nodes) of the afferent fiber, respectively. In both 2D (hair cell and calyx) and 1D (fiber) geometries, local properties such as individual channel conductance density, time constants, and steady state expressions for channel gating variables were defined. Note that the apex of the calyx occurred at 11.3 μm relative to the calyx base for all simulations in the manuscript, except for the variations in calyx height presented in **Fig. 7**.

bioRxiv preprint doi: https://doi.org/10.1101/2021.11.18.469197; this version posted April 29, 2022. The copyright holder for this preprint (which was not certified by peer review) is the author/funder. All rights reserved. No reuse allowed without permission.

Finite Element Mesh in Comsol

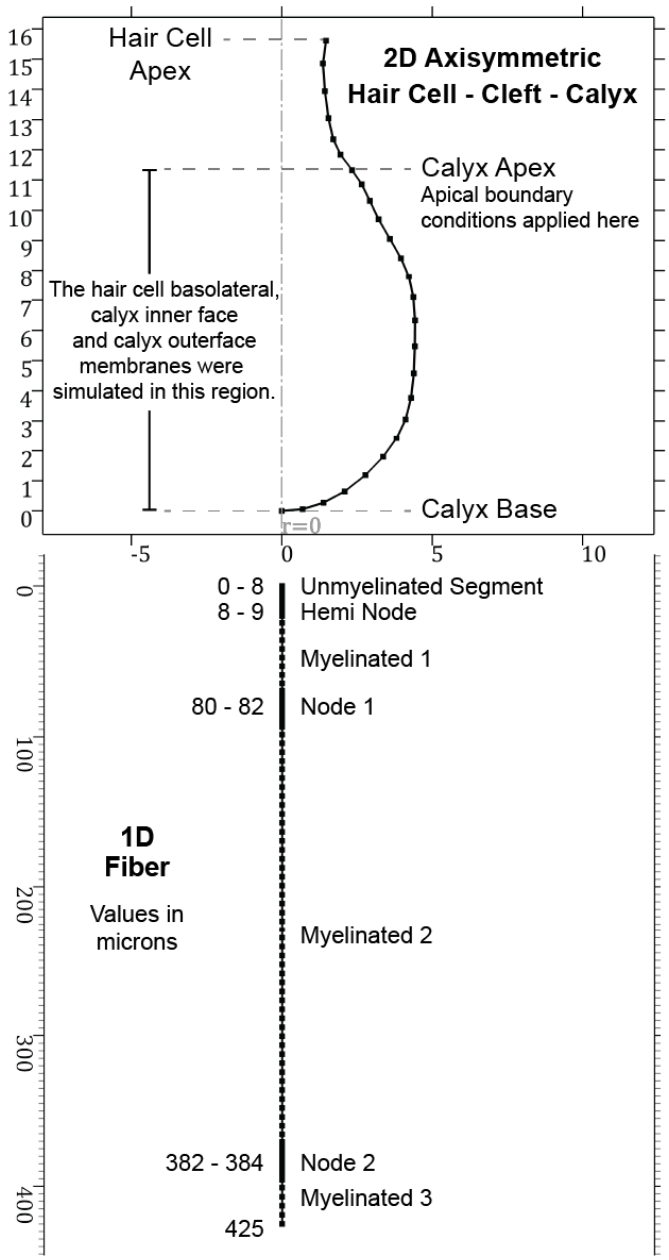

Geometric Parameters

Hair-Cell-Calyx Geometry Interpolation Points	
R (μm)	**Z (μm)**
1.47	15.61 (Hair-Cell Apex)
1.39	14.33
1.5	13.44
1.61	12.72
1.89	11.94
2.33	11.33 (Calyx Apex)
3.16	9.8
4.03	8.28
4.42	5.24
4.03	2.83
2.56	1
1.72	0.43
0	0 (Calyx Base)

Calculated Areas	Values
a_H	340.21 μm^2
$a_{H,C}$	294.63 μm^2
a_{CIF}	294.63 μm^2
a_{COF}	288.33 μm^2
$a_{F,HN}$	3π μm^2
$a_{F,N}$	6π μm^2
$a_{F,Unmyel}$	24π μm^2

Cleft width (d_{SC})	0.02 μm
Calyx width (d_C)	1 μm
Fiber Radius (r_F)	1.5 μm

Fig. S1 – Hair-Cell-Calyx and Fiber Geometries in the COMSOL 5.6 GUI.

The 2D axisymmetric mesh representing the hair cell, synaptic cleft and calyx (top) was modelled based on the geometry of a type I hair-cell-calyx synapse from central/striolar zones of rodent vestibular organs. Dots in the above geometry represent finite element nodes, and lines represent connecting edge elements. The interpolation points were based upon the geometry of a hair cell and calyx reported in Fig. 2C of Lysakowski et al. (2011). d_C was obtained from the same calyx. d_{SC} was obtained from Spoendlin (1966). The fiber radius (r_f) is based on experimental measurements (Lysakowski et al. 1995; Hoffman and Honrubia 2002). The fiber end was treated as a closed boundary. Location of the hemi-node and the first node were estimated from confocal micrographs (Lysakowski et al. 2011). $a_{H,C}$ denotes the surface area of the hair cell within the calyx.

bioRxiv preprint doi: https://doi.org/10.1101/2021.11.18.469197; this version posted April 29, 2022. The copyright holder for this preprint (which was not certified by peer review) is the author/funder. All rights reserved. No reuse allowed without permission.

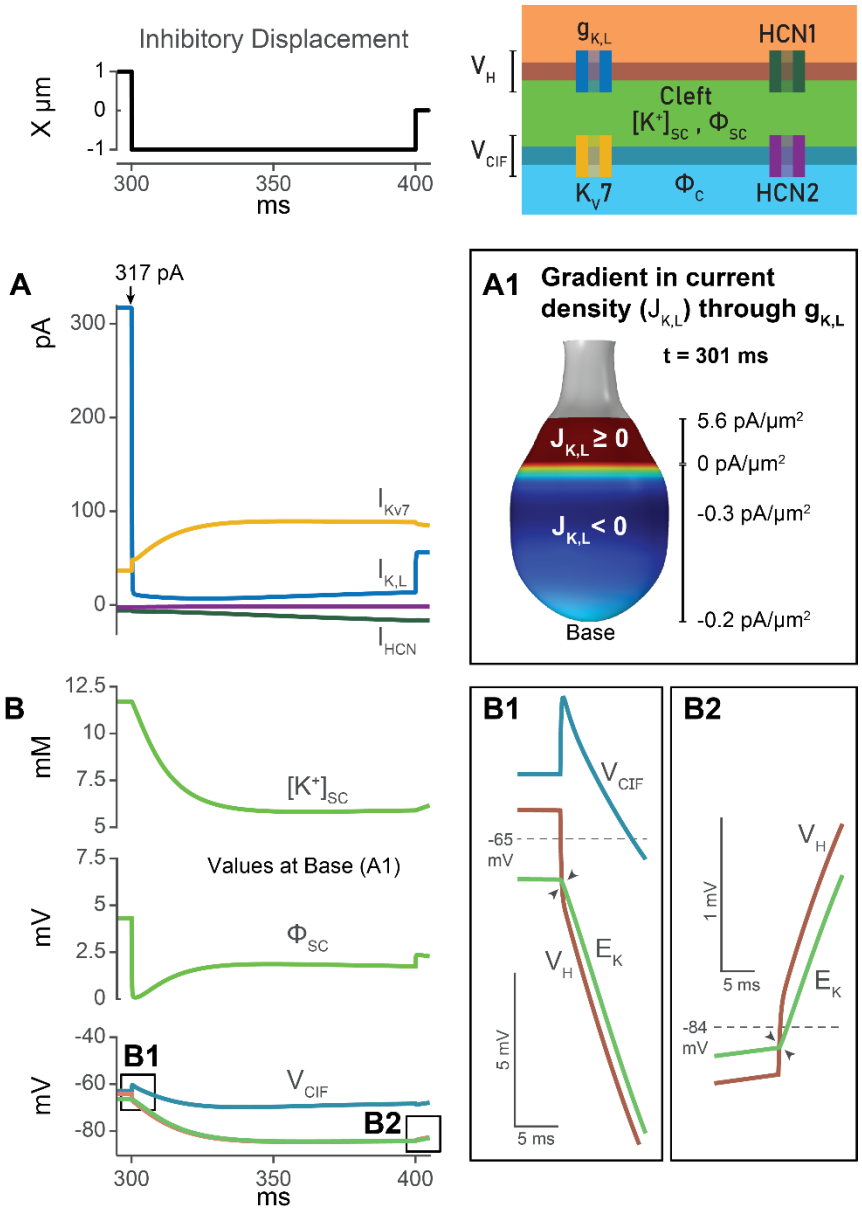

Fig. S2 – Gradients in current density exist from base to apex of the synaptic cleft.

A, Net currents through $g_{K,L}$ (hair cell, blue), K_V7 (calyx, gold) and HCN channels (hair cell, dark green, and calyx, purple) following the onset of the full negative step. **A1,** Gradient in current density through $g_{K,L}$ 1 ms after the negative step at 300 ms. Small currents flow into the hair cell in basal regions, and larger currents flow out of the hair cell near the apical regions of the synaptic cleft. The direction and magnitude of the current results from the difference between V_H and E_K which varies from base to apex and with the ongoing stimulus. This behavior is illustrated at the base of the synapse in B, B1 and B2.

B, $[K^+]_{SC}$, ϕ_{SC}, V_H, V_{CIF} and E_K at the base of the synapse during inhibitory stimuli. Note the crossover of V_H and E_K following the onset (**B1**) and the termination (**B2**) of the negative step. As the driving force for currents is (V_H - E_K), the separation between the V_H and E_K curves determines current magnitude and current direction is outward if V_H is positive to E_K. During the negative step current through $g_{K,L}$ in the basal regions in A1 are inward because V_H is negative to E_K.

bioRxiv preprint doi: https://doi.org/10.1101/2021.11.18.469197; this version posted April 29, 2022. The copyright holder for this preprint (which was not certified by peer review) is the author/funder. All rights reserved. No reuse allowed without permission.

Table S1 - Abbreviations

$\boldsymbol{H}, \boldsymbol{C}, \boldsymbol{SC}, \boldsymbol{CIF}, \boldsymbol{COF}, \boldsymbol{F}$	Subscripts denote the hair cell (*H*), calyx (*C*), synaptic cleft (*SC*), calyx inner face (*CIF*), calyx outer face (*COF*) and fiber (*F*) respectively.
$\boldsymbol{\phi_H}, \boldsymbol{\phi_C}, \boldsymbol{\phi_{SC}}, \boldsymbol{\phi_F}$	Electrical potential in the hair cell, calyx, synaptic cleft and fiber respectively.
$\boldsymbol{\rho_F}$	Resistivity of the afferent fiber. $1/\sigma_F$
$[\boldsymbol{K}^+]_{\boldsymbol{SC}}, [\boldsymbol{Na}^+]_{\boldsymbol{SC}}$	K^+, Na^+ concentrations in the synaptic cleft
$\boldsymbol{c_H}$	Total hair cell capacitance
$\boldsymbol{C_m}$	Specific membrane capacitance
$\boldsymbol{Ca_V}, \boldsymbol{K_V}, \boldsymbol{Na_V}$	Voltage-gated calcium, potassium and sodium channels
$\boldsymbol{D_K}, \boldsymbol{D_{Na}}$	Effective diffusion coefficients for K^+, Na^+ in the synaptic cleft
$\boldsymbol{d_{SC}}$	Width of the synaptic cleft
$\boldsymbol{g_{x,max}}$	Maximum whole-cell conductance of specific channel type
$\boldsymbol{G_{x,max}}$	Maximum conductance density of specific channel type
$\boldsymbol{g_{K,L}}$	Low-voltage-activated potassium conductance of type I hair cells
$\boldsymbol{HCN}$	Hyperpolarization-activated nucleotide-gated (channels)
$\boldsymbol{I_{MET}}$	Mechanotransduction current
$\boldsymbol{J_x}$	Current density through channel or transporter 'x'
J_{M_x}	Current density through membrane 'x'
$\boldsymbol{KCC}$	Potassium Chloride Cotransporter
$\boldsymbol{K_V7}$	Voltage-gated potassium channels formed by subunits encoded by the KCNQ gene family
$\boldsymbol{P_{open}}$	Channel open probability
$\boldsymbol{VHCC}$	Vestibular Hair Cell-Calyx
$\boldsymbol{V_m}$	Membrane voltage

bioRxiv preprint doi: https://doi.org/10.1101/2021.11.18.469197; this version posted April 29, 2022. The copyright holder for this preprint (which was not certified by peer review) is the author/funder. All rights reserved. No reuse allowed without permission.

Table S2 – Equilibrium Potentials and Voltages Across Membranes

Property			Hair Cell (H)	Calyx inner face (CIF)	Calyx outer face (COF)	Fiber (F) HN|N|M
E_K	K^+ Equilibrium Potential	mV	$26 \cdot ln\left(\frac{[K^+]_{SC}}{150}\right)$	$26 \cdot ln\left(\frac{[K^+]_{SC}}{150}\right)$	$26 \cdot ln\left(\frac{[K^+]_{SC}}{150}\right) = -88.4$	-88.4
E_{Na}	Na^+ Equilibrium Potential	mV	$26 \cdot ln\left(\frac{[Na^+]_{SC}}{12}\right)$	$26 \cdot ln\left(\frac{[Na^+]_{SC}}{12}\right)$	$26 \cdot ln\left(\frac{140}{12}\right) = 63.8$	63.8
V_m	Membrane Voltage	mV	$\phi_H - \phi_{SC}$	$\phi_C - \phi_{SC}$	ϕ_C	ϕ_F

bioRxiv preprint doi: https://doi.org/10.1101/2021.11.18.469197; this version posted April 29, 2022. The copyright holder for this preprint (which was not certified by peer review) is the author/funder. All rights reserved. No reuse allowed without permission.

General Modeling of Membrane Currents

Membrane channels and transporters were distributed in the various compartments based on experimental observations (**Table S6, S7**). Abbreviations used for ion channels and other parameters are listed in **Table S1**. For each type of ion, local current density through a particular channel type 'x' was described by **Eq. S1**:

$$J_{ion,x} = G_{x,max} \cdot P_{x,open} \cdot (V_m - E_{ion}) \quad \text{(S1)}$$

$G_{x,max}$ is the maximum conductance density through a channel 'x' per unit area of membrane, obtained by dividing the maximum whole-cell conductance, $g_{x,max}$, by the surface area of the relevant membrane. $P_{x,open}$, calculated as a function of channel gating variables using the Hodgkin-Huxley formalism, is the percentage of the maximal conductance available. The equations describing the kinetics of channel gating variables as functions of membrane voltage and current densities through each channel type are available in **Table S6**. V_m is the transmembrane potential as defined in **Table S2** for each membrane in the model. E_{ion} is the equilibrium potential of the ion species across the membrane and is continuously updated as the ion concentration changes in the synaptic cleft. In the notation for current densities, K, Na, O, indicate the potassium, sodium, and other ions such as Ca^{2+} or Cl^-. Current densities and fluxes, J, through channels and transporters were summed to describe the current densities of ionic species across Hair cell (H) and Calyx Inner Face (CIF) or Calyx Outer Face (COF) membranes. The species currents were in turn summed to obtain the total current densities through each membrane (J_{M_H} , $J_{M_{CIF}}$, $J_{M_{COF}}$, J_{M_F}) (**Table S3**).

See **Table S6** for equations of current densities and kinetics for each channel type.

Table S3– Local and Net Current Densities Across Individual Membranes

$\boldsymbol{J_{K_H}}$	$J_{K,L} + J_{K,HCN1} + J_{K,NaK}$	$\boldsymbol{J_{Na_{CIF}}}$	$J_{Na,HCN2} + J_{Na,NaK}$	$\boldsymbol{J_{M_H}}$	$J_{K_H} + J_{Na_H} + J_{O_H}$
$\boldsymbol{J_{Na_H}}$	$J_{Na,HCN1} + J_{Na,NaK}$	$\boldsymbol{J_{O_{CIF}}}$	$-J_{KCC4}$	$\boldsymbol{J_{M_{CIF}}}$	$J_{K_{CIF}} + J_{Na_{CIF}} + J_{O_{CIF}}$
$\boldsymbol{J_{O_H}}$	J_{Ca}	$\boldsymbol{J_{K_{COF}}}$	$J_{K,HCN2} + J_{K,NaK}$	$\boldsymbol{J_{M_{COF}}}$	$J_{K_{COF}} + J_{Na_{COF}} + J_{Leak}$
$\boldsymbol{J_{K_{CIF}}}$	$J_{K_V7.4} + J_{K_V11.1} + J_{K,HCN2} + J_{K,NaK} + J_{KCC4}$	$\boldsymbol{J_{Na_{COF}}}$	$J_{Na,HCN2} + J_{Na,NaK}$	$\boldsymbol{J_{M_F}}$	$J_{K_V7.x} + J_{K_V1.x} + J_{K_V3.4} + J_{Na_V1.x}$

bioRxiv preprint doi: https://doi.org/10.1101/2021.11.18.469197; this version posted April 29, 2022. The copyright holder for this preprint (which was not certified by peer review) is the author/funder. All rights reserved. No reuse allowed without permission.

Governing Equations

Continuity equations describe the electric potential and ion concentrations in the various compartments.

Hair Cell Electrical Potential (ϕ_H). The time dependence of the hair cell electrical potential is calculated as a function of hair cell capacitance (c_H), mechanotransduction current (I_{MET}), and current across the basolateral membrane:

$$c_H \frac{\partial \phi_H}{\partial t} = -I_{MET} - \int_0^L 2\pi r \left(J_{M_H} - C_m \frac{\partial \phi_{SC}}{\partial t} \right) ds \tag{S2}$$

I_{MET} is calculated according to an instantaneous current-displacement relationship (Holt et al. 1997) and a maximal conductance of 5 nS, based on ~50 transduction channels of ~100-pS single-channel conductance (Corey et al. 2019). We calculated the total capacitance of the hair cell ($c_H = 6.4\, pF$) by multiplying the surface area of the cell by the specific capacitance of the membrane (C_m).

Concentration and Electro-diffusion in the Synaptic Cleft. $[K^+]_{SC}$ and $[Na^+]_{SC}$ were calculated with the Nernst-Planck electro-diffusion equation for each ion:

$$\frac{\partial [K^+]_{SC}}{\partial t} = \nabla \cdot (D_K \nabla [K^+]_{SC}) + \nabla \cdot (D_K \frac{F}{RT} [K^+]_{SC} \nabla \phi_{SC}) + \frac{1}{d_{SC}} \frac{(J_{K_H} + J_{K_{CIF}})}{F} \tag{S3}$$

$$\frac{\partial [Na^+]_{SC}}{\partial t} = \nabla \cdot (D_{Na} \nabla [Na^+]_{SC}) + \nabla \cdot (D_{Na} \frac{F}{RT} [Na^+]_{SC} \nabla \phi_{SC}) + \frac{1}{d_{SC}} \frac{(J_{Na_H} + J_{Na_{CIF}})}{F} \tag{S4}$$

D_K, the effective diffusion coefficient for K^+, is calculated by dividing the diffusion coefficient of K^+ in aqueous solution at $25\,°C$: $1.957 \cdot 10^{-9}\, \frac{m^2}{s}$ (Lide 2005) by the square of the tortuosity coefficient 1.55 (Nicholson and Phillips 1981), $D_K = 0.81 \cdot 10^{-9} \frac{m^2}{s}$. Similarly, $D_{Na} = 0.56 \cdot 10^{-9} \frac{m^2}{s}$. The volume of the synaptic cleft is assumed to be constant and the width (d_{SC}) and length of the synaptic cleft are fixed.

Electrical Potential in the Synaptic Cleft (ϕ_{SC}). At bouton synapses, the electrical potential in the synaptic cleft, ϕ_{SC}, is assumed to be that of the extracellular medium (at reference potential or ground, ~0 mV) because the resistance of the cleft is assumed to be low. At the VHCC synapse, in contrast, the extended synaptic cleft created by the calyx geometry poses an increased resistance and large K^+ currents that flow during transduction may allow a significant cleft potential. ϕ_{SC} was calculated following the law of charge conservation as a function of the resistive and capacitive currents across both pre-synaptic (hair cell) and post-synaptic (calyx) membranes, as well as electro-diffusion of ions:

bioRxiv preprint doi: https://doi.org/10.1101/2021.11.18.469197; this version posted April 29, 2022. The copyright holder for this preprint (which was not certified by peer review) is the author/funder. All rights reserved. No reuse allowed without permission.

$$(2C_m)\frac{d\phi_{SC}}{dt} = C_m\frac{d\phi_H}{dt} + C_m\frac{d\phi_{Calyx}}{dt} + J_H + J_{CIF} + \nabla\cdot(FD_K\nabla[K^+]_{SC})\cdot d_{SC} + \nabla\cdot(FD_{Na}\nabla[Na^+]_{SC})\cdot d_{SC} + \nabla\cdot\left(\left(\sigma_{O_{SC}} + \frac{D_K\,[K^+]_{SC}\,F^2}{RT} + \frac{D_{Na}\,[Na^+]_{SC}\,F^2}{RT}\right)\nabla\phi_{SC}\right)\cdot d_{SC} \quad \text{(S5)}$$

At room temperature, the terms $\frac{D_K\,[K^+]_{SC}\,F^2}{RT} + \frac{D_{Na}\,[Na^+]_{SC}\,F^2}{RT}$ resolve to ~ 300 - 400 nS/µm when $[K^+]_{SC}$ and $[Na^+]_{SC}$ range between 5-40 and 120-140 mM, respectively. The total conductivity contribution from ions ($\sigma_{O_{SC}}$) other than K^+ and Na^+ is set equal to 600 nS/µm to be consistent with the 1000 nS/µm used in the calyx and afferent fiber. 1000 nS/µm (equivalent to 1 S/m) is within the conductivity range (0.75 – 1.45 S/m) reported from measurements in tumor cells (Wang et al. 2017), hippocampal neurons (Zhou et al. 2016) and cerebrospinal fluid (Baumann et al. 1997). The diffusion of other ions, e.g., chloride, was not explicitly considered and their concentrations within the synaptic cleft are assumed to be constant and a part of the $\sigma_{O_{SC}}$ term.

Electrical Potential in the Calyx (ϕ_C). The electrical potential within the calyx was calculated as a function of the resistive and capacitive currents across both the post-synaptic membrane and the calyx outer face membranes as well as the longitudinal current from the afferent fiber.

$$(2C_m)\frac{d\phi_C}{dt} = C_m\frac{d\phi_{SC}}{dt} + \nabla\cdot(\sigma_C d_C\,\nabla\phi_C) - J_{\mathrm{CIF}} - J_{\mathrm{COF}} - J_F \quad \text{(S6)}$$

The current from the fiber to the calyx, J_F, is equal to $(-\pi\cdot\frac{r_f}{\rho_l}\cdot u_x)$, where r_f the radius of the fiber is 1.5 µm, ρ_l the longitudinal resistivity is 1 MΩ µm, and u_x is the longitudinal potential gradient within the fiber. The fiber radius used is comparable to diameters reported for calyx afferents (Hoffman and Honrubia 2002).

Electrical Potential in the Afferent Fiber (ϕ_F). To describe the potential in the afferent fiber, ϕ_F, we implemented the cable equation along the 1D line representing the fiber:

$$r_F^2\frac{d^2\phi_F}{dx^2} = 2r_F\rho_l C_m\frac{d\phi_F}{dt} - 2r_F\rho_F J_{M_F} \quad \text{(S7)}$$

Channel gating variables and conductance densities (see **Table S6**) were defined for the hemi-node, nodes and myelinated regions of the fiber as shown in **Fig. 1**. Gating variables for channels present on the fiber were treated similarly to those on the calyx and hair cell.

bioRxiv preprint doi: https://doi.org/10.1101/2021.11.18.469197; this version posted April 29, 2022. The copyright holder for this preprint (which was not certified by peer review) is the author/funder. All rights reserved. No reuse allowed without permission.

Initial and Boundary Conditions. Before running the simulation, the initial value of ϕ_H was set at -70 mV, within the normal range of reported resting potentials for rodent type I hair cells (Rennie and Correia 1994; Rennie et al. 1996; Rüsch and Eatock 1996; Chen and Eatock 2000; Lim et al. 2011; Spaiardi et al. 2017). Where necessary, initial values of ϕ_H were varied $\pm$10 mV to assist solver convergence. An initial value of 0 mV was used for the potential in the synaptic cleft, ϕ_{SC}. The boundary condition $\phi_{SC} = 0$ mV was applied at the apical end of the synaptic cleft. An initial value of –70 mV was used for ϕ_{Calyx} and ϕ_F, consistent with recorded resting potentials in rodent calyces ranging –60 to –70 mV in (Meredith and Rennie 2015; Sadeghi et al. 2014; Songer and Eatock 2013). The boundary condition $\phi_{Calyx} = \phi_F$ was applied at the base of the calyx and the far end of the fiber was treated as a closed boundary. $[K^+]_{SC}$ and $[Na^+]_{SC}$ were given initial values of 5 mM and 140 mM, respectively, throughout the cleft, based on the external (bath) recording solutions of electrophysiological data referenced in the model and similar to perilymph facing the outer face of the calyx and other extracellular salines. K^+ and Na^+ concentrations were pinned at these values at the apical end of the cleft but were allowed to vary elsewhere within the cleft. To better understand Non-quantal Transmission (NQT), we altered the initial conditions to independently analyze the contributions of changes in the synaptic cleft in (1) electrical potential and (2) potassium concentration. As described below, this theoretical exercise gave greater insight into the mechanisms of NQT.

bioRxiv preprint doi: https://doi.org/10.1101/2021.11.18.469197; this version posted April 29, 2022. The copyright holder for this preprint (which was not certified by peer review) is the author/funder. All rights reserved. No reuse allowed without permission.

Table S4 – Initial and Boundary Conditions

Parameter	Value	Reference
$\phi_{H,init}$	-75 mV	(Correia and Lang 1990; Rennie and Correia 1994; Rennie et al. 1996; Rüsch and Eatock 1996; Chen and Eatock 2000; Lim et al. 2011; Spaiardi et al. 2017)
$\phi_{SC,init}$	0 mV	Based on the external (bath) recording solutions of electrophysiological data referenced in the model
$\phi_{SC,apical}$	0 mV	
$[K^+]_{SC,init}$ $[K^+]_{SC,apical}$	5 mM	
$[Na^+]_{SC,init}$ $[Na^+]_{SC,apical}$	140 mM	
$\phi_{C,init}$	-70 mV	(Meredith and Rennie 2015; Sadeghi et al. 2014; Songer and Eatock 2013)
$\phi_{F,init}$	-70 mV	Assumed continuous with $\phi_{C,init}$

ϕ_{SC}-Only Condition. To isolate the contribution of changes in electrical potential within the synaptic cleft to NQT, we held ion concentrations in the synaptic cleft constant at 5 mM for $[K^+]_{SC}$ and 140 mM $[Na^+]_{SC}$ (**Eqs. S3 and S4**) and removed terms for ion diffusion in the cleft from **Eq. S5**.

$$(2C_m)\frac{d\phi_{SC}}{dt} = C_m\frac{d\phi_H}{dt} + C_m\frac{d\phi_C}{dt} + J_{\mathrm{H}} + J_{\mathrm{CIF}} + \nabla \cdot \left(\left(\sigma_{O_{SC}} + \frac{D_K[K^+]_{SC}F^2}{RT} + \frac{D_{Na}[Na^+]_{SC}F^2}{RT}\right)\nabla\phi_{SC}\right)\cdot d_{SC} \tag{S8}$$

$$\frac{\partial[K^+]_{SC}}{\partial t} = 0\,;\ [K^+]_{SC} = 5\,mM \tag{S9}$$

$$\frac{\partial[Na^+]_{SC}}{\partial t} = 0;\ [Na^+]_{SC} = 140\,mM \tag{S10}$$

$[K^+]_{SC}$-Only Condition. To isolate the contribution of changes in K^+ concentration in the synaptic cleft to NQT, we fixed ϕ_{SC} at 0 mV and removed the electrical drift terms in **Eqs. S3 and S4**.

$$(2C_m)\frac{d\phi_{SC}}{dt} = 0\,;\ \phi_{SC} = 0\,mV \tag{S11}$$

bioRxiv preprint doi: https://doi.org/10.1101/2021.11.18.469197; this version posted April 29, 2022. The copyright holder for this preprint (which was not certified by peer review) is the author/funder. All rights reserved. No reuse allowed without permission.

$$\frac{\partial[K^+]_{SC}}{\partial t} = \nabla \cdot (D_K \nabla[K^+]_{SC}) + \frac{1}{d_{SC}} \frac{(J_{K_H} + J_{K_{CIF}})}{F} \tag{S12}$$

$$\frac{\partial[Na^+]_{SC}}{\partial t} = \nabla \cdot (D_{Na} \nabla[Na^+]_{SC}) + \frac{1}{d_{SC}} \frac{(J_{Na_H} + J_{Na_{CIF}})}{F} \tag{S13}$$

Model Simulation and Solver Conditions

In the COMSOL 5.6 software, the finite element mesh was generated based on geometric parameters for the hair-cell-calyx and fiber (**Fig. S1**). The number and distribution of finite element nodes (hair-cell-calyx: 26 nodes, 25 edge elements; fiber: 95 nodes, 94 edge elements) was chosen to minimize error in the solutions of the governing equations. To obtain the resting conditions, we ran the model simulation with a stationary solver. For a step or sinusoidal displacement of the hair cell's stereociliary bundle or hair cell voltage steps, we used a time-dependent solver to determine the responses in the hair cell, synaptic cleft, calyx and afferent fiber. The time-dependent solver was run using the backward difference formula (BDF) method. The temporal resolution (maximum time step) was: 1 ms for resting conditions before stimulus onset; 0.01 ms from 1 ms before stimulus onset to 10 ms after stimulus onset; and 0.1 ms for all other intervals. The model simultaneously solves **Eqs. S1-S7** to simulate the electrical potential of the hair cell and the spatiotemporal evolution of electrical potential, potassium concentration, sodium concentration in the synaptic cleft, and potential in the afferent fiber.

bioRxiv preprint doi: https://doi.org/10.1101/2021.11.18.469197; this version posted April 29, 2022. The copyright holder for this preprint (which was not certified by peer review) is the author/funder. All rights reserved. No reuse allowed without permission.

Table S5 – Conductances, Diffusion Coefficients and Capacitances

σ_C	1000 nS/µm	(Baumann et al. 1997; Geddes and Baker 1967; Zhou et al. 2016; Wang et al. 2017)
C_m	0.01 pF/µm^2	(Curtis and Cole 1938; Gentet et al. 2000)
$C_{m,Myel}$	0.00002 pF/µm^2	(Stämpfli 1954)
D_K	0.81 µm/ms	(Lide 2005). See methods near **Eq. S4**
D_{Na}	0.56 µm/ms	(Lide 2005). See methods near **Eq. S4**
$g_{bundle,max}$	5 nS	(Holt et al. 1997)
$g_{Ca,max}$	0.5 nS	(Bao et al. 2003)
$g_{HCN1,max}$	4.2 nS	(Horwitz et al. 2011)
$g_{HCN2,max}$	3.6 nS	(Horwitz et al. 2014)
$g_{K,L,max}$	80 nS	(Spaiardi et al. 2017)
$g_{K_V7.4,max}$	24 nS	(Hurley et al. 2006)
$g_{K_V1.x,max}$	6.3 nS	(Kalluri et al. 2010)
$G_{K_V3.4,max}$	0.2 nS/µm^2	(Chabbert et al. 2001)
$g_{K_V7.x,max}$	4.5 nS	(Kalluri et al. 2010)
$g_{Na_V,unitary}$	10 pS	(Bezanilla 1987; Kay et al. 1998)
ρ_{Na_V}	12,000/µm^2	(Ritchie and Rogart 1977)

bioRxiv preprint doi: https://doi.org/10.1101/2021.11.18.469197; this version posted April 29, 2022. The copyright holder for this preprint (which was not certified by peer review) is the author/funder. All rights reserved. No reuse allowed without permission.

Channel Distribution and Kinetics

The governing equations depend upon the net current densities across the pre- and post-synaptic membranes in the model. The constitutive currents and their kinetics as used in the model are detailed in **Table S6**. All channel properties used were from electrophysiological measurements near room temperature (23 – 27°C). For a given channel, $act_{\infty}(V)$ and $\tau_{act}(V)$ are expressions for the dependence of the activation 'act' (or inactivation 'inact') gating variable on the membrane voltage and the corresponding time constant. $act(t)$ is the instantaneous value of the gating variable. The expressions for $act(V)$ and $\tau_{act}(V)$ were stored in variables assigned to the VHCC and fiber geometry to make them locally available during model evaluation. The maximum whole-cell conductance value $g_{x,max}$ for any type of channel 'x' was divided by the surface area to obtain the maximum conductance density $G_{x,max}$ to allow us to evaluate local current densities at specific sites in the model. The transporters Na^+/K^+-ATPase and KCC were assumed to operate at pseudo-steady state and depend only on $[K^+]$ in the cleft. On the hair cell, basolateral channels were only distributed to the part of the membrane enclosed by the calyx.

Table S6. Currents Densities and Kinetics

MET (Hair Cell Apical)

$$I(X) = g_{bundle,max} \cdot P_{MET} \cdot \left(\phi_H - V_{bundle,rev} - \phi_{endolymph}\right)$$

$$P_{MET} = \left(1 + exp\left(4.05 \cdot \left(0.39 - \frac{X+200}{1000}\right)\right)\right)^{-1} \cdot \left(1 + exp\left(14.5 \cdot \left(0.25 - \frac{X+200}{1000}\right)\right)\right)^{-1}$$

$X = displacement(t)$; Step or sinusoidal functions were used.

Kinetics in the model: (Holt et al. 1997).
$V_{bundle,rev}$, the reversal voltage is 0 mV (Corns et al. 2014).
$\phi_{endolymph}$ is 5 mV (Köppl et al. 2018; Li et al. 2020).

$g_{K,L}$ (Hair Cell)

$$J_{K,L} = G_{K,L,max} \cdot P_{K,L} \cdot (V_m - E_K)$$

$$G_{K,L,max} = \frac{g_{K,L,max}}{a_{H,C}}$$

$$P_{K,L} = act_{K,L}$$

$$\tau_{K,L} \cdot \frac{d\left(act_{K,L}\right)}{dt} = act_{\infty,K,L} - act_{K,L}$$

$$\tau_{K,L} = 429.7 \cdot exp\left(-0.2826 \cdot \frac{V_m - (-80)}{2.84}\right) + 10$$

bioRxiv preprint doi: https://doi.org/10.1101/2021.11.18.469197; this version posted April 29, 2022. The copyright holder for this preprint (which was not certified by peer review) is the author/funder. All rights reserved. No reuse allowed without permission.

$$act_{\infty,K,L} = \left(1 + exp\left(-\frac{V_m - (-80)}{2.84}\right)\right)^{-1}$$

Presence in hair cell: (Rennie and Correia 1994; Rüsch and Eatock 1996).
Activation Kinetics in the model: (Spaiardi et al. 2017, 2020).
$\tau_{K,L}$ is based on measurements of the slow time constant: (Wong et al. 2004; Songer and Eatock 2013; Spaiardi et al. 2017).

g_{Ca} (Hair Cell)

$$J_{Ca} = G_{Ca,max} \cdot P_{Ca} \cdot (V_m - E_{Ca})$$

$$G_{Ca,max} = g_{Ca,max} \,/\, a_{H,C}$$

$$P_{Ca} = act_{Ca}$$

$$\tau_{Ca} \cdot \frac{d(act_{Ca})}{dt} = act_{\infty,Ca} - act_{Ca}$$

$$\tau_{Ca} = 0.6\, ms$$

$$act_{\infty,Ca} = \frac{1}{1 + \exp\left(-\frac{V_m - (-44)}{5.8}\right)}$$

Presence and Kinetics: (Bao et al. 2003), assuming an intracellular $[Ca^{2+}]$ of $1\mu M$.

HCN1 (Hair Cell)

$$J_{K,HCN1} = \frac{4}{5} \cdot G_{HCN1,max} \cdot P_{HCN1} \cdot (V_m - E_K)$$

$$J_{Na,HCN1} = \frac{1}{5} \cdot G_{HCN1,max} \cdot P_{HCN1} \cdot (V_m - E_{Na})$$

$$G_{HCN1,max} = g_{HCN1,max} \,/\, a_{H,C}$$

$$P_{HCN1} = act_{HCN1}$$

$$\tau_{HCN1} \cdot \frac{d(A_{HCN1})}{dt} = act_{\infty,HCN1} - act_{HCN1}$$

$$\tau_{HCN1} = 209.479 + \frac{\left(exp\left(-\frac{V_m + 80.646}{6.916}\right)\right)^{-1} + exp\left(\frac{V_m + 80.646}{14.881}\right)}{2551.988}$$

$$act_{\infty,HCN1} = \frac{1}{1 + exp\left(\frac{V_m - (-90))}{6.8}\right)}$$

Location and Kinetics: (Horwitz et al. 2014), adapted for simple calyx.
τ_{HCN2}: (Ventura and Kalluri 2019), Parameters for the HCN "Max Activation" case.
The K^+ : Na^+ permeability ratio through HCN1 channels is 4:1 (Lee and MacKinnon 2017). The fractions 4/5 and 1/5 in the equations for $J_{K,HCN1}$, and $J_{Na,HCN1}$ reflect this.

bioRxiv preprint doi: https://doi.org/10.1101/2021.11.18.469197; this version posted April 29, 2022. The copyright holder for this preprint (which was not certified by peer review) is the author/funder. All rights reserved. No reuse allowed without permission.

Na^+/K^+-ATPase (Hair Cell | Calyx Inner Face | Calyx Outer Face)

$$J_{pump} = (3-2) \cdot \frac{F \cdot 10^{12}}{N_A} \cdot \rho_{NaK} \cdot v_{NaK} \cdot P_{pump}$$

$\rho_{NaK} =$ 1000 | 1000 | 2000 pumps/μm^2

$$P_{pump} = \left(\frac{[K^+]_{SC}}{[K^+]_{SC}+1.5}\right)^2 \Bigg| \left(\frac{[K^+]_{SC}}{[K^+]_{SC}+1.5}\right)^2 \Bigg| \left(\frac{5}{5+1.5}\right)^2;$$

Presence of Na^+/K^+-ATPase: (Schuth et al. 2014).
A pseudo-steady state expression was used with v_{NaK} of 100/s, a Hill coefficient of 2 (Jaisser et al. 1994) and a K^+ molar affinity of 1.5 mM, adapted from (Crambert et al. 2000). ρ_{NaK} values were chosen such that the $[Na^+]_{SC}$ at rest, at the base of the cleft, was between 120 – 140 mM with the reasoning that quantal currents occurring at the calyx inner face would require sufficient Na^+ driving forces. In the expression for J_{pump}, 10^{12} is a conversion factor from Coulombs to picoCoulombs.

KCC4 (Calyx Inner Face)

$$J_{KCC4} = J_{KCC4,max} \cdot P_{KCC4}$$

$J_{KCC4,max}$ = 2 pA/μm^2

$$P_{KCC4} = \left(1 + \left(\frac{17.5}{[K^+]_{SC}}\right)^2\right)^{-1}$$

Molar affinity (17.5 mM) from (Mercado et al. 2000). Hill Coefficient based on discussions in (Marcoux et al. 2017). $J_{KCC4,max}$ was chosen such that the $[K^+]_{SC}$ at rest, at the base of the cleft as calculated by the stationary solver was between 5-7 mM. Although J_{KCC4} is expressed as a current, transport activity of KCC is electroneutral and does not contribute to a change in potential. KCC4 was localized to the calyx inner face, see Experimental Methods below.

$K_V7.4$ (Calyx Inner Face | Calyx Outer Face)

$$J_{K_V7.4} = G_{K_V7.4,max} \cdot P_{K_V7.4} \cdot (V_m - E_K)$$

$$G_{K_V7.4,max} = \frac{\frac{4}{5} g_{K_V7.4,max}}{a_{CIF}} \mid \frac{\frac{1}{5} g_{K_V7.4,max}}{a_{COF}}$$

$$P_{K_V7.4} = act_{K_V7.4}$$

$$\tau_{K_V7.4} \cdot \frac{d(act_{K_V7.4})}{dt} = act_{\infty,K_V7.4} - act_{K_V7.4}$$

$$\tau_{K_V7.4} = max\left(\left(0.0002488 \cdot exp(-0.04401 \cdot V_m) + 0.4506 \cdot exp(0.05437 \cdot V_m)\right)^{-1}, 1\right)$$

$$act_{\infty,K_V7.4} = \left(1 + exp\left(\frac{V_m - (-52)}{16}\right)\right)^{-1}$$

bioRxiv preprint doi: https://doi.org/10.1101/2021.11.18.469197; this version posted April 29, 2022. The copyright holder for this preprint (which was not certified by peer review) is the author/funder. All rights reserved. No reuse allowed without permission.

Location & Kinetics: (Hurley et al. 2006).
In $G_{K_V7.4,max}$, the fractions 4/5 and 1/5 reflect the relative density of the channel on either membrane observed in electron microscope immunogold experiments. See Experimental Methods below.

HCN2 (Calyx Inner Face | Calyx Outer Face)

$$J_{K,HCN2} = \frac{4}{5} \cdot G_{HCN2,max} \cdot P_{HCN2} \cdot (V_m - E_K)$$

$$J_{Na,HCN2} = \frac{1}{5} \cdot G_{HCN2,max} \cdot P_{HCN2} \cdot (V_m - E_{Na})$$

$$G_{HCN2,max} = \frac{\frac{1}{2} g_{HCN2,max}}{a_{CIF}} \mid \frac{\frac{1}{2} g_{HCN2,max}}{a_{COF}}$$

$g_{HCN2,max}$ was distributed equally to both the CIF and COF.

$$P_{HCN2} = act_{HCN2}$$

$$\tau_{HCN2} \frac{d(act_{HCN2})}{dt} = act_{\infty,HCN2} - act_{HCN2}$$

$$\tau_{HCN2} = 209.479 + \left(\left(exp\left(-\frac{V_m + 80.646}{6.916} \right) \right)^{-1} + exp\left(\frac{V_m + 80.646}{14.881} \right) \right) / 2551.988$$

$$act_{\infty,HCN2} = \left(1 + exp\left(\frac{V_m + 95}{11.7} \right) \right)^{-1}$$

Presence and Kinetics: (Horwitz et al. 2014). Adapted for a simple calyx.
τ_{HCN2}: (Ventura and Kalluri 2019), Parameters for the HCN "Max Activation" case.
The K^+ : Na^+ Permeability ratio through HCN1 channels is 4:1 (Lee and MacKinnon 2017). The same ratio was assumed for HCN2 channels. The fractions 4/5 and 1/5 in the equations for $J_{K,HCN2}$, and $J_{Na,HCN2}$ reflect this.

I_{Leak} (Calyx Outer Face)

$$J_{Leak} = G_{Leak,max} \cdot (V_m - 0)$$

$$G_{Leak,max} = \frac{g_{Leak,max}}{a_{COF}}$$

$g_{Leak,max}$ was set equal to 2 nS. The value was chosen to compensate for unknown membrane properties and assist in setting the resting calyx potential.

$K_V7.x$ (Hemi-Node | Node)

$$J_{K_V7.x} = G_{K_v7.x,max} \cdot P_{K_V7.x} \cdot (V_m - E_k)$$

bioRxiv preprint doi: https://doi.org/10.1101/2021.11.18.469197; this version posted April 29, 2022. The copyright holder for this preprint (which was not certified by peer review) is the author/funder. All rights reserved. No reuse allowed without permission.

$$G_{K_v7.x,max} = \frac{g_{K_V7.x,max}}{a_{F,HN} + 2a_{F,N}}$$
$$P_{K_V7.x} = act_{K_V7.x}$$
$$\tau_{K_V7.x} \cdot \frac{d\left(act_{K_V7.x}\right)}{dt} = act_{\infty,K_V7.x} - act_{K_V7.x}$$
$$\tau_{K_V7.x} = 1.2 \cdot exp(-0.08 \cdot V_m) \cdot \frac{1}{1 + exp\left(-\frac{V_m + 47}{8}\right)}$$
$$act_{\infty,K_V7.x} = \frac{1}{1 + exp\left(-\frac{V_m + 47}{8}\right)}$$

Kinetics: (Kalluri et al. 2010).

K_V3.4 (Hemi-Node | Node)

$$J_{K_V3.4} = G_{K_V3.4,max} \cdot P_{K_V3.4} \cdot (V_m - E_k)$$
$$P_{K_V3.4} = act_{K_V3.4} \cdot inact_{K_V3.4}$$
$$\tau_{K_V3.4,act} \cdot \frac{d\left(act_{K_V3.4}\right)}{dt} = act_{\infty,K_V3.4} - act_{K_V3.4}$$
$$\tau_{K_V3.4,inact} \cdot \frac{d\left(inact_{K_V3.4}\right)}{dt} = inact_{\infty,K_V3.4} - inact_{K_V3.4}$$
$$\tau_{K_V3.4,act} = 5 \cdot 1.41 \cdot exp(-0.05589 \cdot V_m) \cdot \left(1 + exp\left(-\frac{V_m+31.3}{8.5}\right)\right)^{-1}$$
$$\tau_{K_V3.4,inact} = 25.4 \text{ ms}$$
$$act_{\infty,K_V3.4} = \left(1 + exp\left(-\frac{V_m+31.3}{8.5}\right)\right)^{-1}$$
$$inact_{\infty,K_V3.4} = \left(1 + exp\left(\frac{V_m+65.84}{5.51}\right)\right)^{-1}$$

Kinetics: (Chabbert et al. 2001). $G_{K_V3.4,max}$ was adapted to a value of 0.2 nS/µm^2 and is comparable to the values for $G_{K_V1.x,max}$ and $G_{K_V7.x,max}$.

K_V1.x (Hemi-Node | Node)

$$J_{K_V1} = G_{K_V1,max} \cdot P_{K_V1} \cdot (V_m - E_k)$$
$$G_{K_v1.x,max} = \frac{g_{K_V1.x,max}}{a_{F,HN} + 2a_{F,N}}$$
$$P_{K_V1} = act_{K_V1}$$
$$\tau_{K_V1} \cdot \frac{d\left(act_{K_V1}\right)}{dt} = act_{\infty,K_V1} - act_{K_V1}$$
$$act_{\infty,K_V1} = \frac{1}{1 + exp\left(-\frac{V_m + 44}{7.1}\right)}$$
$$\tau_{K_V1} = 3.7\ ms$$

Kinetics: (Kalluri et al. 2010).

bioRxiv preprint doi: https://doi.org/10.1101/2021.11.18.469197; this version posted April 29, 2022. The copyright holder for this preprint (which was not certified by peer review) is the author/funder. All rights reserved. No reuse allowed without permission.

Na_v (Unmyelinated|Hemi-Node | Node)

$J_{Na_V} = G_{Na_V,max} \cdot P_{Na_v} \cdot (V_m - E_{Na})$

$J_{Na_V,Unmyel} = \frac{1}{4} \cdot G_{Na_V,max} \cdot P_{Na_v} \cdot (V_m - E_{Na})$

$G_{Na_V,max} = g_{Na_V,unitary} \cdot \rho_{Na_V}$

$P_{Na_V} = act_{Na_V} \cdot inact_{Na_V}$

$\tau_{Na_V,act} \cdot \frac{d(act_{Na_V})}{dt} = act_{\infty,Na_V} - act_{Na_V}$

$\tau_{Na_V,inact} \cdot \frac{d(inact_{Na_V})}{dt} = inact_{\infty,Na_V} - inact_{Na_V}$

$\tau_{Na_V,act} = \left(1 + \exp\left(-\frac{V_m + 41.58}{5.733}\right)\right)^{-1} \cdot \left(1 + \exp\left(\frac{V_m + 8.295}{16.28}\right)\right)^{-1} + 0.2$

(for -55 $\leq V_m \leq 60\ mV$); 0.2 ms otherwise.

$\tau_{Na_V,inact} = 0.0001452\ exp(-0.2211\ V_m) + 0.2382$

(for -45 $\leq V_m \leq 60\ mV$); else, linearly extrapolated.

$act_{\infty,Na_V} = \left(1 + exp\left(-\frac{V_m+40}{8}\right)\right)^{-1}$

$inact_{\infty,Na_V} = \left(1 + exp\left(\frac{V_m+69}{7.6}\right)\right)^{-1}$

Kinetics: (Liu et al. 2016; Meredith and Rennie 2018).
$\tau_{Na_V,act}$ and $\tau_{Na_V,inact}$, see Experimental Methods below.

A reduced channel density was assumed at the unmyelinated segment and the maximum conductance density reduced to ¼ of the full value. This reflects evidence for greater channel clustering near regions adjacent to myelinated segments of fiber (Freeman et al. 2016).

bioRxiv preprint doi: https://doi.org/10.1101/2021.11.18.469197; this version posted April 29, 2022. The copyright holder for this preprint (which was not certified by peer review) is the author/funder. All rights reserved. No reuse allowed without permission.

Table S7 - Sources

Model Compartment	Property	Reference	Animal	Location	Age
General	Calyx Dimensions	(Lysakowski et al. 2011) Fig. 2C – central calyx-only afferent	Rat	SCC	6 Months
Hair Cell	MET	(Holt et al. 1997)	Mouse	Utricle	P1 - P10
	MET, P_0 = 10%	(Songer and Eatock 2013)	Rat	Saccule	P1 - P9
	MET, 5nS	(Holt et al. 1997)	Mouse	Utricle	P1 - P10
	$g_{K,L}$	(Spaiardi et al. 2017)	Mouse	SCC	P6 - P19
	$\tau_{g_{K,L}}$	(Wong et al. 2004)	Rat	Utricle	P16 - P24
	Fit of slow time constant	(Songer and Eatock 2013)	Rat	Saccule	P1 – P9
		(Spaiardi et al. 2017)	Mouse	SCC	P6 - P19
	gCa	(Bao et al. 2003)	Rat	SCC	P4 - P20
	HCN1	(Horwitz et al. 2011)	Mouse	Utricle	P0 - P25
HC/Calyx	Na^+/K^+-ATPase	(Schuth et al. 2014)	Rat	Utricle/SCC	P17– P25
	τ_{HCN}	(Ventura and Kalluri 2019) - HCN Max Activation parameters	Rat	VGN	P9 - P21
Calyx	HCN2	(Horwitz et al. 2014)	Mouse	Utricle	P0 - P25
	$K_v7.4$	(Hurley et al. 2006)	Rat	Utricle	P2 - P26
		(Lysakowski et al. 2011)	Rat	Utricle/SCC	6 Months
	KCC4	See Experimental Methods	Rat	SCC	6 months
		(Mercado et al. 2000)	Frog Oocyte	(expressing mouse KCC4)	Day 5
		(Marcoux et al. 2017)	Various mammals	-	-
Fiber	HN, N1 Location	(Lysakowski et al. 2011)	Rat	Utricle, Saccule and SCC	6 Months

bioRxiv preprint doi: https://doi.org/10.1101/2021.11.18.469197; this version posted April 29, 2022. The copyright holder for this preprint (which was not certified by peer review) is the author/funder. All rights reserved. No reuse allowed without permission.

Na_V	(Liu et al. 2016)	Rat	VGN	P1 - P8
	(Meredith and Rennie 2018)	Gerbil	SCC	P5 - P31
K_v7	(Kalluri et al. 2010)	Rat	VGN	P8 - P15
K_v1	(Kalluri et al. 2010)	Rat	VGN	P8 - P15
$K_v3.4$	(Chabbert et al. 2001)	Mouse	VGN	P5 - P8

SCC – Semicircular Canal Crista. Utricle and saccule reference their maculae. Conductance values are presented in **Table S5** and kinetics are presented in **Table S6**.

bioRxiv preprint doi: https://doi.org/10.1101/2021.11.18.469197; this version posted April 29, 2022. The copyright holder for this preprint (which was not certified by peer review) is the author/funder. All rights reserved. No reuse allowed without permission.

EXPERIMENTAL METHODS

Below we describe the experimental methods used to determine unpublished parameters listed in the Tables, and imaged cells shown in **Fig. 1A**.

Na_V time constants (Table S6):

Whole-cell patch clamp recordings from mouse vestibular afferent neurons. The kinetics of postsynaptic (afferent) Na_V currents were obtained from mouse vestibular ganglion neurons isolated in the first postnatal month. Animals were handled in accordance with the *National Institutes of Health Guide for the Care and Use of Laboratory Animals*, and all procedures were approved by the animal care committee at the University of Chicago. Mice were deeply anesthetized with isoflurane and decapitated. Vestibular ganglia were dissected out and mechanically dissociated following enzymatic digestion (with 0.12% collagenase and 0.12% trypsin for 15-20 minutes at 37°C) and cultured overnight to remove satellite cells, in minimal essential medium with Glutamax (MEM, Invitrogen, Carlsbad, CA) supplemented with 10 mM HEPES, 5% fetal bovine serum (FBS), and 1% penicillin in 5% CO_2-95% air at 37°C. Whole-cell patch clamp recordings were made with solutions designed to minimize contamination from K^+ and Ca^{2+} currents. The external medium comprised (mM): 75 NaCl, 5.4 CsCl, 2.5 $MgCl_2$, 75 TEACl, 5 HEPES, 10 D-glucose, titrated with CsOH to pH 7.4, with osmolality ~310 mmol/kg. The internal (pipette) solution contained: 148 CsCl, 0.8 CaCl, 3.5 Na_2-creatine phosphate, 3.5 MgATP, 0.1 LiGTP, 5 EGTA, 5 HEPES, 0.1 Na-cAMP, titrated with CsOH to pH 7.4, and ~300 mmol/kg. Recordings were made at room temperature (23-25°C). Signals were delivered and recorded with a Multiclamp 700B amplifier, Digidata 1440A digitizer, and pClamp 10 or 11 software (Axon Instruments, Molecular Devices, Sunnyvale, CA), with low-pass Bessel filtering set at 10 kHz and sampling interval set at 5 µs. Seal resistance exceeded 1 GΩ. Membrane voltages were corrected off-line for a measured liquid junction potential of 6.4 mV and for series resistance errors. Analysis was performed with MATLAB (The MathWorks, Natick, MA), Clampfit (Axon Instruments, Molecular Devices) and Origin Pro 2018 (OriginLab, Northampton, MA). Series resistance (R_S) ranged between 3 and 10 MΩ and was compensated by 75%. The holding potential was −66.4 mV. Activation and inactivation time courses were measured for currents evoked by depolarizing voltage steps following a pre-pulse to −127 mV to de-inactivate Na_V current. The currents were fit with the following Hodgkin-Huxley equations for Na_V channel activation (n=6) and inactivation (n=9):

$$I(t) = I_{peak}\left(1 - e^{-\frac{t}{\tau_m}}\right)^3; I(t) = I_{SS} + I_{peak}(e^{-t/\tau_h})$$

where I is current, t is time; I_{peak} and I_f are peak and steady-state (inactivated) currents, respectively; and τ_m and τ_h are the time constants for the activation and inactivation transitions, respectively.

bioRxiv preprint doi: https://doi.org/10.1101/2021.11.18.469197; this version posted April 29, 2022. The copyright holder for this preprint (which was not certified by peer review) is the author/funder. All rights reserved. No reuse allowed without permission.

Location of KCC, relative density of K_V7.4 (Table S6) and image of hair cells and calyces (Fig. 1A): Confocal microscopy and immunocytochemistry

Fixation. Animals were handled in accordance with the *National Institutes of Health Guide for the Care and Use of Laboratory Animals*, and all procedures were approved by the IACUC at the Univ. of Illinois at Chicago. Long-Evans rats (Charles River Laboratories, Wilmington, MA) were deeply anesthetized with Nembutal (80 mg/kg), then perfused transcardially for 1 min with physiological saline containing heparin (2000 IU), followed by a dialdehyde fixative for 10 min (4% paraformaldehyde, 1% acrolein, 1% picric acid, and 5% sucrose in 0.1 M phosphate buffer (PB), pH 7.4). After decapitation, the head was post-fixed in the fixative for 20 min and then placed in 30% sucrose in 0.1 M PB. Vestibular and auditory organs were dissected out with the head immersed in PB. Decalcification of cochleas and removal of bone debris and otoliths from vestibular organs was accomplished through incubation in Cal-X solution. Background fluorescence was reduced by incubating the tissues in a 1% aqueous solution of sodium borohydride for 10 min. All organs were then placed in 30% sucrose in 0.1 M PB overnight.

Immunohistochemistry. Dissected tissues were gelatin-embedded and cut with a freezing sliding microtome. Tissue permeabilization was carried out with 4% Triton X-100 in PBS for 1 hr, and a blocking solution composed of 0.5% fish gelatin, 0.5% Triton X-100 and 1% BSA in 10 mM phosphate-buffered saline (PBS) was used for 1 hr. Samples were incubated in primary antibodies diluted 1:200 in blocking solution: goat anti-calretinin (AB1550), rabbit anti-KCC4 (AB3270) (all available or formerly available from Chemicon/Millipore-Sigma, St. Louis, MO) or rabbit anti-myosin 6 (a generous gift from Dr. Tama Hasson). The anti-calretinin antibody served as a marker of type II hair cells and calyx afferents (Desai et al. 2005). Specific labeling was revealed with these secondary antibodies (1:200 in the blocking solution): FITC-conjugated donkey anti-goat and rhodamine-conjugated donkey anti-rabbit (both from Chemicon, Temecula, CA). Sections were mounted on slides using a medium containing Mowiol (Calbiochem, Darmstadt, Germany) and examined on a confocal microscope (LSM 510 META, Carl Zeiss, Oberköchen, Germany). The relative density of Kv7.4 channels was based on electron microscopic (EM) immunogold experiments, with methods described in Hurley et al. (2006). In brief, 40-μm vibratome sections were incubated in primary antibody [1:200 rabbit anti-KCNQ4, a generous gift from Dr. Bechara Kachar] for 72 h and secondary antibody (1:50; colloidal gold-labeled goat anti-rabbit IgG; Amersham Biosciences, Piscataway, NJ) for 24 h. Colloidal gold staining was silver enhanced (4–8 min; IntenSE M kit; Amersham Biosciences). For more details, see Hurley et al. (2006).